

The impact of spectroscopic incompleteness in direct calibration of redshift distributions for weak lensing surveys

W. G. Hartley,^{1,2,3,*} C. Chang,^{4,5} S. Samani,¹ A. Carnero Rosell,⁶ T. M. Davis,⁷ B. Hoyle,^{8,9} D. Gruen,^{10,11,12} J. Asorey,⁶ J. Gschwend,^{13,14} C. Lidman,¹⁵ K. Kuehn,^{16,17} A. King,⁷ M. M. Rau,¹⁸ R. H. Wechsler,^{10,11,12} J. DeRose,^{19,20} S. R. Hinton,⁷ L. Whiteway,¹ T. M. C. Abbott,²¹ M. Aguena,^{13,22} S. Allam,²³ J. Annis,²³ S. Avila,²⁴ G. M. Bernstein,²⁵ E. Bertin,^{26,27} S. L. Bridle,²⁸ D. Brooks,¹ D. L. Burke,^{11,12} M. Carrasco Kind,^{29,30} J. Carretero,³¹ F. J. Castander,^{32,33} R. Cawthon,³⁴ M. Costanzi,^{35,36} L. N. da Costa,^{13,14} S. Desai,³⁷ H. T. Diehl,²³ J. P. Dietrich,³⁸ B. Flaugher,²³ P. Fosalba,^{32,33} J. Frieman,^{23,5} J. García-Bellido,²⁴ E. Gaztanaga,^{32,33} D. W. Gerdes,^{39,40} R. A. Gruendl,^{29,30} G. Gutierrez,²³ D. L. Hollowood,²⁰ K. Honscheid,^{41,42} D. J. James,⁴³ S. Kent,^{23,5} E. Krause,⁴⁴ N. Kuropatkin,²³ O. Lahav,¹ M. Lima,^{22,13} M. A. G. Maia,^{13,14} J. L. Marshall,⁴⁵ P. Melchior,⁴⁶ F. Menanteau,^{29,30} R. Miquel,^{16,47} R. L. C. Ogando,^{13,14} A. Palmese,^{23,5} F. Paz-Chinchón,^{29,30} A. A. Plazas,⁴⁶ A. Roodman,^{11,12} E. S. Rykoff,^{11,12} E. Sanchez,⁶ V. Scarpine,²³ M. Schubnell,⁴⁰ S. Serrano,^{32,33} I. Sevilla-Noarbe,⁶ M. Smith,⁴⁸ M. Soares-Santos,⁴⁹ E. Suchyta,⁵⁰ G. Tarle,³¹ M. A. Troxel,⁵¹ D. L. Tucker,²³ T. N. Varga,^{8,9} J. Weller,^{8,9} and R.D. Wilkinson⁵²

(DES Collaboration)

(affiliations are listed at the end of the paper)

* Corresponding author: william.hartley@unige.ch

29 May 2022

ABSTRACT

Obtaining accurate distributions of galaxy redshifts is a critical aspect of weak lensing cosmology experiments. One of the methods used to estimate and validate redshift distributions is apply weights to a spectroscopic sample so that their weighted photometry distribution matches the target sample. In this work we estimate the *selection bias* in redshift that is introduced in this procedure. We do so by simulating the process of assembling a spectroscopic sample (including observer-assigned confidence flags) and highlight the impacts of spectroscopic target selection and redshift failures. We use the first year (Y1) weak lensing analysis in DES as an example data set but the implications generalise to all similar weak lensing surveys. We find that using colour cuts that are not available to the weak lensing galaxies can introduce biases of $\Delta z \sim 0.015$ in the weighted mean redshift of different redshift intervals. To assess the impact of incompleteness in spectroscopic samples, we select only objects with high observer-defined confidence flags and compare the weighted mean redshift with the true mean. We find that the mean redshift of the DES Y1 weak lensing sample is typically biased at the $\Delta z = 0.005 - 0.05$ level after the weighting is applied. The bias we uncover can have either sign, depending on the samples and redshift interval considered. For the highest redshift bin, the bias is larger than the uncertainties in the other DES Y1 redshift calibration methods, justifying the decision of not using this method for the redshift estimations. We discuss several methods to mitigate this bias.

Key words: cosmology: distance scale – galaxies: distances and redshifts – galaxies: statistics – large scale structure of Universe – gravitational lensing: weak

1 INTRODUCTION

Over the last decade, a number of new deep imaging surveys have been developed in order to take advantage of the cosmological information contained within the distortion of galaxy shapes by weak gravitational lensing. One of the quantities required to be known in order to unlock this information is

the distribution in redshift of the galaxies whose light is being distorted. The first of the so-called stage III programmes (Albrecht et al. 2006) designed to measure weak lensing have now been completed (Heymans et al. 2013; Joudaki et al. 2017). Current state-of-the-art surveys, such as the Kilo-Degree Survey (KiDS, de Jong et al. 2015), the Hyper SuprimeCam Sur-

vey (HSC, Aihara et al. 2017) and the Dark Energy Survey (DES, Flaugher, Diehl et al. 2015) can now achieve levels of cosmological parameter constraints competitive with those from cosmic microwave background observations (DES Collaboration et al. 2019).

In order to reach such precision, the redshift distribution of the weak lensing source galaxies, and in particular the mean redshift of any tomographic redshift interval, must be very precisely constrained. In Hoyle, Gruen et al. (2018, hereafter H18), we estimated that, in the four tomographic bins chosen for the weak lensing cosmology analysis with the first year of DES survey data (redshift binning $0.2 < z < 0.43$, $0.43 < z < 0.63$, $0.63 < z < 0.9$, and $0.9 < z < 1.3$), the mean redshifts are known to Gaussian uncertainties of 0.016, 0.013, 0.011, and 0.022 respectively. The anticipated scale of the full DES survey data implies that these uncertainties need to be reduced by roughly a factor of five, else they will overwhelm the statistical errors. Forthcoming experiments (LSST¹, Euclid², and WFIRST³) require yet more stringent precision and accuracy.

In this context, a long literature has developed, describing approaches to derive redshift distributions (Mandelbaum et al. 2008; Hildebrandt et al. 2012; Benjamin et al. 2013; Schmidt & Thorman 2013; Rau et al. 2015), validate them (Sánchez et al. 2014; Bonnett et al. 2016; Choi et al. 2016; Hildebrandt et al. 2018; Hoyle et al. 2018; Tanaka et al. 2018; Wright et al. 2018) and overcome some of the expected challenges in doing so (Newman 2008; Rau et al. 2017; Buchs et al. 2019; Sánchez & Bernstein 2019). A natural approach to validation is to use the very precise redshifts that can be obtained from spectroscopic observations of some of the science-sample galaxies, and almost all methods for deriving photometric redshift distributions are tested in this way. The principal challenges in validating with spectroscopy are mis-assigned spectroscopic redshifts (Cunha et al. 2014; Newman et al. 2015), colour and magnitude-dependent differences in sampling rate (Lima et al. 2008) and field-to-field variance effects (Cunha et al. 2012). The first challenge is effectively solved by using only the highest confidence redshift determinations, transferring the problem to a greater imbalance in sampling rate.

Lima et al. (2008) presented an algorithm for estimating the redshift distribution of a target photometric sample from a spectroscopic data set directly, by accounting for the differences in sampling. It amounts to estimating the density of objects in the locale (in data space – e.g. colour-magnitude space, including scatter due to photometric errors) of each spectroscopic data point, in both the spectroscopic sample itself and in the target data. The ratio of these densities is then given as a weight to the spectroscopic object. Finally, the redshift distribution is recovered by creating a weighted histogram of the spectroscopic sample. In addition to accounting for differences in sampling rate, weighting in this way also reduces the impact of field-to-field variance (e.g. H18).

In recent applications to weak lensing cosmology, this approach of weighting a spectroscopic sample has been used as either an independent measure of the redshift distribution (Bonnett et al. 2016), or as the leading redshift solution (the so-called “direct calibration”, or DIR method, Hildebrandt et al. 2018; Joudaki et al. 2019; Asgari et al. 2019). Insofar as a full and direct validation of photometric redshifts with spectroscopy goes, this weighting scheme is the only technique

Table 1. Characteristics of the main spectroscopic samples used in the DES Y1 analysis.

Survey	Number of spectra	mean redshift	total weight
VVDS	11,121	0.60	0.15
VIPERS	9,455	0.58	0.13
DEEP2	7,167	0.96	0.13
zCOSMOS	11,751	0.54	0.13
WiggleZ	13,496	0.57	0.10
3D-HST	7,011	0.86	0.10
ACES	4,244	0.58	0.08
OzDES	12,436	0.61	0.06
eBOSS _{ELG}	4,322	0.96	0.03

employed in weak lensing analyses to date. One of the main requirements for using direct weighting of spectroscopic samples is that the spectroscopic data set must cover the same colour-magnitude space as the target sample (weak lensing sources, for example). However, there is the further assumption being made when taking such an approach, that within any given region of the colour-magnitude space the spectroscopic redshifts are representative of the local true redshift distribution of the lensing source sample. In general, there is no reason for this assumption to hold true. In any region of colour-magnitude space there will be some width to the redshift distribution — perhaps due to photometric errors or insufficient dimensionality to the data. It is not difficult to conceive of situations in which low and high confidence redshift determinations in that region have systematically different redshifts.

In Bonnett et al. (2016) we used existing spectroscopic and photometric datasets, similar to those considered in this paper, and showed that regions of colour-magnitude space that have poor spectroscopic success rates ($< 65\%$) are on average biased by $\Delta z \sim 0.03$ with respect to the COSMOS photometric redshifts of a weak-lensing-like selection. This bias drops to $\Delta z \sim 0.01$ for regions with higher completeness. Similarly, work from Gruen & Brimiouille (2017) found that there exist significant biases (up to $\Delta z = 0.1$) in terms of the mean redshift, with the worst cases occurring at greatest depth. In this work we take one step further and investigate the origin of this bias. We assess, via spectroscopic simulations, the magnitude of the bias in terms of the mean redshift of the inferred redshift distributions for a target photometric sample (designed to mimic a weak lensing survey). We use DES as an example but the principle can be applied to other experiments.

The paper is structured as follows. In Sec. 2 we describe the full procedure in constructing redshift distributions from a simulated spectroscopic sample. The target sample for which we wish to construct redshift distributions is the weak lensing sample for the first year of DES data (DES Y1). We describe the simulated spectra constructed from a full N -body simulation, the process of redshifting the spectra and determine the confidence level, enlarging the sample with a random forest approach, and ultimately reweighting the spectroscopic sample to match the photometry of the target sample. In Sec. 3 we present our findings in terms of the bias in the mean redshift in tomographic bins introduced via the incompleteness in the spectroscopic sample. We demonstrate first with VIPERS as an example of how targetting strategies introduce incompleteness, and then with a spectroscopic sample similar to that in DES Y1. In Sec. 4 we dis-

¹ www.lsst.org

² <http://sci.esa.int/euclid/>

³ <https://wfirst.gsfc.nasa.gov/>

cuss three potential mitigation approaches of this bias and estimate their performances. We conclude in Sec. 5.

2 RECONSTRUCTING THE REDSHIFT DISTRIBUTIONS VIA A SIMULATED SPECTROSCOPIC SAMPLE

In this section, we simulate the full process involved in constructing the principal spectroscopic samples that overlap the DES Y1 footprint and that would be used to obtain redshift distributions in a DIR-like method. Below we first describe the spectroscopic data we aim to simulate (Sec. 2.1). Then we introduce the set of galaxy simulations that our work is built upon (Sec. 2.2). Next we describe how we simulate the observed spectra (Sec. 2.3) as well as the process of having human “redshifters” visually inspect the simulated spectra and assign them quality flags (Sec. 2.4). Next, we train a random forest (RF) on these simulated spectra and assign quality flags to generate a larger dataset (Sec. 2.5). The RF sample is then reweighted so that the photometry is matched to the target sample (Sec. 2.6) where we could compare the redshift distribution with the truth. Finally we discuss the various simplifications in this procedure and how they might affect our main results (Sec. 2.7).

2.1 Overview of spectroscopic data in DES

We use DES Y1 as an example survey to study in this paper, though the principle that we explore is applicable to any similar experiment. The DES Y1 weak lensing analysis carried out in DES Collaboration et al. (2019); Troxel et al. (2018) used 26 million source galaxies to place unprecedented constraints on cosmological parameters. The basis of the redshift distribution of these source galaxies used in that analysis is detailed in H18.

Table 1 and Appendix A in Bonnett et al. (2016) summarise the spectroscopic samples covered by the deep supernova fields in DES, which serve as calibration fields for the main-survey redshift distributions. As detailed in Sánchez et al. (2014) and Bonnett et al. (2016), these photo- z calibration fields were chosen to overlap with a number of key deep spectroscopic samples. In particular, three of the fields, SN-X1, SN-X3 and SN-C3, are well-studied extra-galactic fields containing VVDS Deep (Le Fèvre et al. 2005), ACES (Cooper et al. 2012) and the rich spectroscopy built up in the SXDS / UKIDSS Ultra-Deep Survey (e.g. Hartley et al. 2013). The other two calibration fields were chosen to overlap with the VVDS Wide F14 field (Garilli et al. 2008) and COSMOS (Scoville et al. 2007), which again provides a large number of spectroscopic samples for training. Overall, the dominant spectroscopic samples used in Bonnett et al. (2016) and H18 are: VVDS, VIPERS (Guzzo et al. 2014), DEEP2 (Newman et al. 2013), zCOSMOS⁴ (Lilly et al. 2009), WiggleZ (Parkinson et al. 2012), 3D-HST (Brammer et al. 2012), ACES, OzDES (Childress et al. 2017) and eBOSS (Dawson et al. 2016). Table 1 lists the major characteristics of these samples. This table motivates the choices of spectroscopic samples we simulate later in this paper. That is, although these samples were not used as the primary redshift calibration method in H18, if DES Y1 were to use a direct redshift calibration method (or, the DNF algorithm, De Vicente et al.

2016), these would form the basis of the spectroscopic sample of choice.

In this paper, we choose to focus on VVDS, VIPERS and zCOSMOS. The data for these three spectroscopic samples were all taken by the same instrument, VIMOS (Le Fèvre et al. 2003), and are three of the four surveys that carry the greatest weight in our DIR-like algorithm.⁵ VVDS is further split into “Wide” and “Deep” fields. We note that due to limitations in our simulations, we will not perform this study with the DEEP2 sample. The DEEP2 sample was taken via the DEIMOS spectrograph (Faber et al. 2003), and has the particular strength of high enough spectral resolution to split the [OII] doublet. The **k-correct** templates used for this work are at lower resolution, cannot replicate that strength and thus would not allow meaningful results to be obtained from our simulations.

2.2 Mock galaxy catalog

The simulated spectroscopic surveys that we produce for our analysis are based on an initial selection from the Buzzard (v1.1) mock galaxy catalog (DeRose et al. 2019, Wechsler et al. in prep). In this set of simulations, three flat Λ CDM dark-matter-only N -body simulations were used, with 1050^3 , 2600^3 and 4000^3 $\text{Mpc}^3 h^{-3}$ boxes and 1400^3 , 2048^3 and 2048^3 particles, respectively. These boxes were run using LGADGET-2 (Springel 2005) with 2LPTic initial conditions from Crocce et al. (2006) and CAMB. The cosmology assumed was $\Omega_m = 0.286$, $\Omega_b = 0.047$, $\sigma_8 = 0.82$, $h = 0.7$, $n_s = 0.96$, and $w = -1$. Particle lightcones were created from these boxes on the fly. Galaxies were then placed into the simulations and *grizY* magnitudes and shapes assigned to each galaxy using the algorithm Adding Density Determined Galaxies to Lightcone Simulations (ADDGALS, Wechsler et al. in prep.). Each galaxy is assigned an SED from SDSS DR6 (Cooper 2006) by finding neighbours in the space of $M_r - \Sigma_5$, where Σ_5 is the projected distance to the fifth nearest neighbor in redshift slices of width $\delta z = 0.02$. These SEDs are k -corrected and represented by five coefficients that correspond to five **k-correct** templates. The spectra are then integrated over the appropriate bandpasses to generate the DES *grizY* photometric magnitudes. A further post-processing step is used to add appropriate photometric errors to the magnitudes according to what is measured in the DES Y1 data.

2.3 Simulated spectroscopic training set

We now wish to construct simulated spectroscopic surveys from the mock galaxy catalog described above. Specifically, this includes simulating the target selection function and the spectra of those targets with the expected signal-to-noise ratio.

As described in Sec. 2.1, the four data sets of interest are: VVDS Deep, VVDS Wide, VIPERS and zCOSMOS. Simple magnitude and colour cuts form the target selection in each of these surveys (see Table 2 for the magnitude and colour cuts used in each sample). Our simulated data contains both noiseless, true photometry and simulated observed photometry, as described in Sec. 2.2. Spectroscopic targeting was performed with the true magnitudes to reflect the fact that typically deeper data was used during the real target selection, and to

⁴ We use “zCOSMOS” to refer to the publicly available zCOSMOS-bright sample at $15 < i < 22.5$.

⁵ Here, “weight” refers to the fraction of the photometric sample that is represented by galaxies in the survey after adjusting for representativeness, following Lima et al. (2008).

Table 2. Observational parameters used to generate the simulated spectra.

Survey	VVDS Wide	VVDS Deep	VIPERS	zCOSMOS
Selection criteria	$17.5 < i < 22.5$	$17.5 < i < 24$	$17.5 < i < 22.5$; $r - i > 0.5(u - g)$ or $r - i > 0.7$	$15 < i < 22.5$
Exposure time (sec)	45	270	45	60
Number of spectra	21550	12932	20452	20689
Sky emission model	ESO VIMOS Exposure Time Calculator			Noll et al. (2013)
Instrument transmission	ESO VIMOS Exposure Time Calculator			Le Fèvre et al. (2003)
Slit loss			30%	
Mirror area (m ²)			51.86	
Star fraction	0.0	0.0	0.0488	0.0633

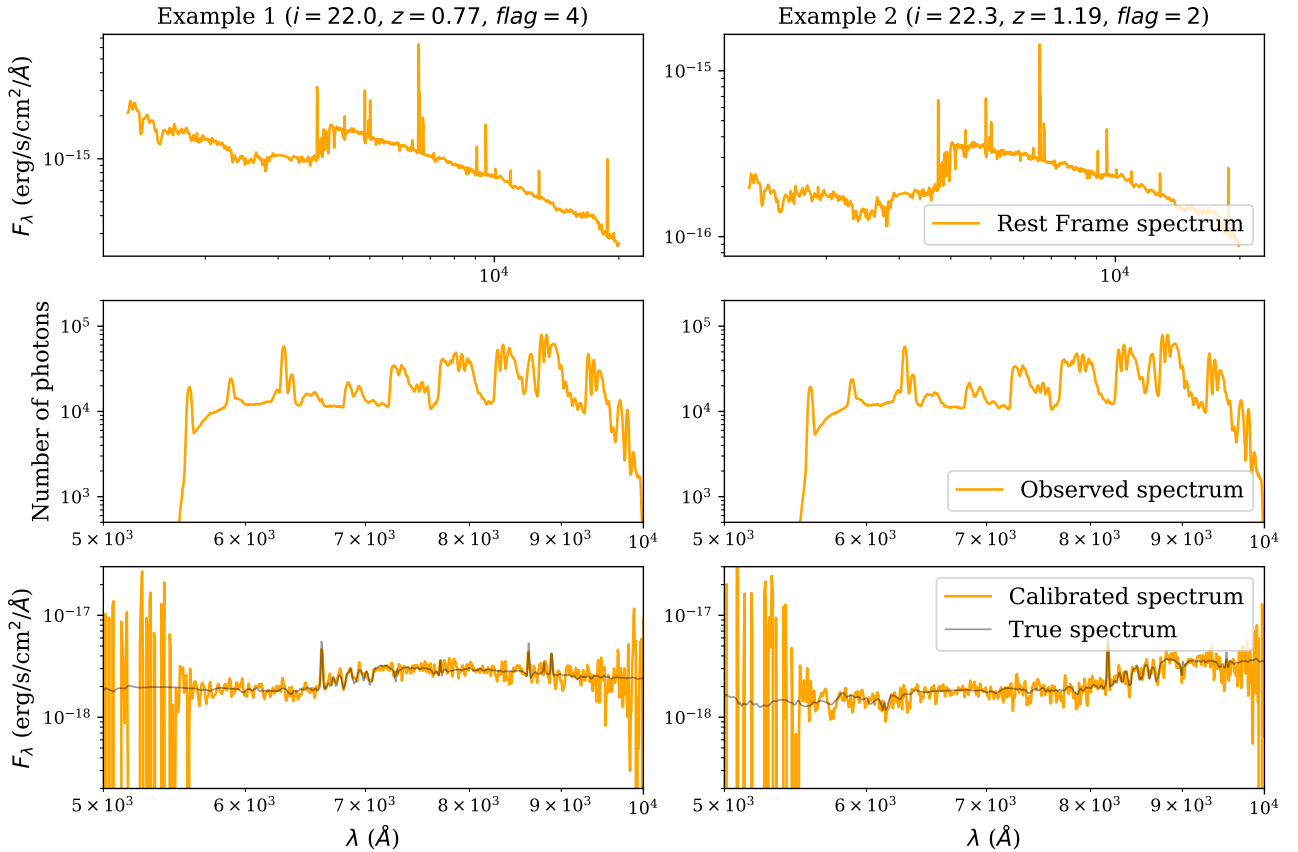


Figure 1. Example spectra from the simulated VVDS Deep survey. **Top panels:** Original rest-frame linear combination of **k-correct** components. **Middle panels:** Poisson-sampled spectrum including sky emission. Note that the apparent shape of the spectrum is dominated by the sky emission. **Bottom panels:** Final sky-subtracted and calibrated simulated spectrum (yellow) overlaid with the true spectrum (black). The former is what is passed onto the next stage for redshifting. The *i*-band magnitudes as well as the true redshifts for the two galaxies are listed at the top of the figure. The spectra on the left represents an example of a good spectrum (Flag=4), while the spectra on the right represent a spectrum of relatively poor quality (Flag=2).

avoid a one-to-one correspondence with the simulated DES photometry (again, to better reflect the real situation). The selections were sampled from areas of sky that are similar to the real survey data, and placed with similar angular separations as the real surveys, in order to capture the appropriate field-to-field variance uncertainties. However, note that this simple selection does not take into account other complexities in a real target selection scenario where e.g. slit mask constraints are an issue.

Next, observational parameters of the different surveys need to be defined. We use the parameters listed in Table 2. These are based on outputs from the ESO exposure time calculator for VIMOS, which uses sky illumination and trans-

mission function defined in Noll et al. (2013) and Le Fèvre et al. (2003) respectively. We choose to apply average values for moon phase (grey) and slit losses (30%) to all objects for simplicity.

To generate a simulated spectrum that mimics the noisy spectra of the real surveys after sky-subtraction and calibration, we start from the mock target list described above and carry through the following steps:

- (i) Multiply **k-correct** templates with coefficients provided in the mock galaxy catalog to get a rest-frame spectrum.
- (ii) Redshift the rest-frame spectrum to the galaxy's red-

shift z so that the spectral flux density at λ is shifted to $(1+z)\lambda$.

(iii) Re-bin the spectrum to the required instrument resolution.

(iv) Convert the flux density into units of photon counts per wavelength bin.

(v) Apply slit-loss factor and transmission.

(vi) Add sky background (which already includes the transmission efficiency).

(vii) Poisson sample the noisy spectrum (including sky).

(viii) Subtract an estimated sky background. In practice, the number of sky pixels in each slit means that this value is close to the true value.

(ix) Divide by the transmission and slit-loss factor to correct for instrument response and flux-calibrate the spectrum.

This process is done for all the objects in all the surveys and packaged into FITS files that could be easily loaded into the redshifting program for the next step. See also Fagioli et al. (2018) for a similar process applied to simulate SDSS spectra.

In Fig. 1 we show two examples of simulated spectra from our simulated VVDS Wide data set. The top panels of Fig. 1 show the noiseless rest-frame spectra. These example objects were chosen to be intrinsically fairly similar galaxies, but with different redshifts and confidence flags (explained in the next section). The middle panels show the “observed” spectra with noise and sky background. It is clear that the sky dominates the signal. The bottom panels show the calibrated spectra following corrections due to the transmission and estimated sky (yellow) and the true spectra (black). We see that the simulated spectra recover the shape of their respective input spectra very well in the range 5500–9900 Å. The galaxy in Example 1 is slightly brighter than that in Example 2, which results in a higher signal-to-noise ratio (S/N) spectrum.

We note that for practical reasons, we have made several simplifications in the above procedure (see a list of simplifications discussed in Sec. 2.7). As a result, we expect the estimation from this analysis to be conservative – further complications of the data should introduce higher redshift biases.

2.4 Redshifting and Quality Flags

The spectroscopic surveys that we aimed to reproduce had redshifts determined by a combination of template cross correlation, emission line detection and a human inspection to confirm or replace those determinations. Importantly, the flags that represent the confidence that a given spectroscopic redshift is correct were all assigned by human observers. To be able to estimate the impact of any selection biases introduced, we must follow as close an approach as is practical and therefore also use human redshift and quality flag determinations.

Redshifting of the simulated spectra was performed by a team of eight observers with mixed levels of experience. Most were familiar either with redshifting optical spectra from AAOmega or VIMOS. Two of the eight had not performed such a task before and of our observers, two performed around 50% of the redshifting. We use the software package **MARZ**⁶ (Manual and Automatic Redshifting Software, Hinton et al. 2016), which is a web-based semi-automated template-fitting application, similar in essence to the commonly used **EZ** program for VIMOS (Garilli et al. 2010). **MARZ** uses a cross-correlation algorithm to match input spectra against a vari-

ety of stellar and galaxy templates in order to solve for the redshift.

We generated a total of 75,623 simulated spectra (the sum of the number of spectra in all the samples in Table 2), and randomly selected 12,000 for the redshifting procedure. These spectra were split into 40 subsamples, and each redshifter examined one or more of these subsamples and returned their results. We did not attempt to redshift all the spectra, as it was impractical to replicate the redshifting of three full VIMOS surveys, but instead choose to train a random forest using these 12,000 spectra and generate the full dataset in Sec. 2.5.

The task for these redshifters is to assign a best redshift and an estimate of how secure they believe that redshift to be in the form of a redshift quality flag. Each flag value corresponds to a different confidence level of the determined redshift:

- Flag=4: essentially 100% certain
- Flag=3: 95 - 99 % certain
- Flag=2: 90 % certain
- Flag=1: 50% certain
- Flag=0: a guess

In addition, there is a special flag 6 (9 in the VVDS scale), which is for cases where there is a clear emission line, but insufficient supporting information to be able to tell which line it is – i.e. there are a small number of possible redshifts, but the values can be quite different from one another. For most of this work we later re-assign these flags as 2.5 because they effectively sit in between flag 2 and 3 in confidence for the purposes of weak lensing experiments. In practice almost all flag 6 objects were given the correct redshift, but because even a small fraction of wrong redshifts can cause biases, such objects are typically not used in analyses on real data.

In the spectra shown in Fig. 1, Example 1 has been given the highest confidence flag. The strong and clear emission line is in a clean part of the spectral range, relatively unaffected by bright sky lines, and easily identified as [OII] based on the abundant supporting information: a break in the continuum, multiple Balmer absorption lines and weak but present [OIII]+H β lines. In contrast, the ambiguity over whether the [OII] line is real or a sky subtraction residual in Example 2, together with the lack of convincing supporting evidence (lower S/N Balmer lines), results in a Flag=2 determination. Had the object been at significantly lower redshift a higher confidence would almost certainly have been assigned. This is a fairly common mode of failure in attempting to obtain a secure redshift. Other typical failure modes include: key emission lines in blue galaxies lying entirely outside of the spectral range, the 4000Å break of red galaxies lying outside of the range (which occurs at both high and very low redshift in the MR and LR-Red grisms) and dust extinction reducing the S/N of emission lines and/or the 4000Å break. Spectra of very low S/N can be problematic too, if they do not happen to have multiple clear emission lines within the spectral window. Finally, observers can occasionally find it difficult to assign confident redshifts if a spectrum presents unexpected features (e.g. those associated with the presence of an AGN), or if it is a blend of two objects at different redshifts. These factors result in a highly complex selection function in the joint space of galaxy type, redshift and luminosity.

The above procedure is clearly not objective. Different redshifters may have different scales in mind when assigning confidence flags to the spectra they inspect. In fact, depending on external environmental conditions, a single observer can change the confidence scale for the same object from one

⁶ <https://samreay.github.io/Marz/>

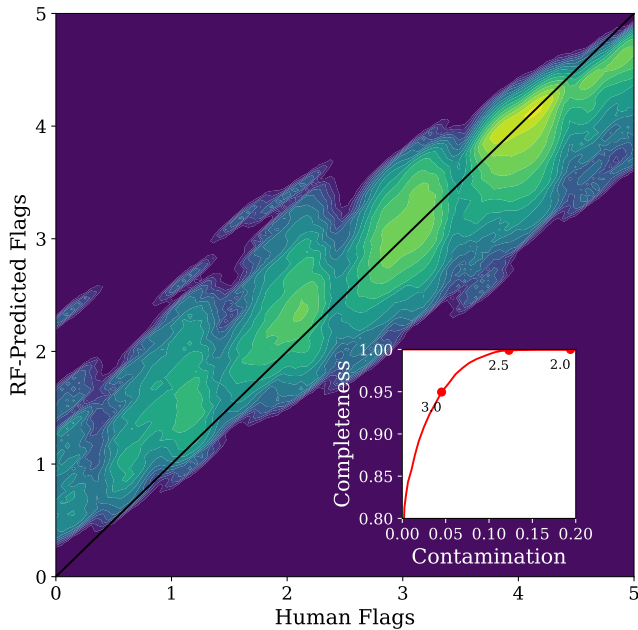


Figure 2. Random forest (RF) prediction of redshift quality flag against those determined by human observers. The mean predicted flags span a smaller range of values than the true flags, while the overall dispersion is of order 1. The bottom right inset shows a Receiver Operating Characteristic (ROC) curve for the completeness of the sample, the numbers indicate flag values – lower flags would result in larger completeness and higher contamination.

sitting to the next. In the real surveys that our simulations are based on, each spectrum was inspected by more than one observer and an arbitration procedure was followed in the case of conflicts in redshift and/or quality flags. While it cannot guarantee uniformity across a large data set, this process at least helps to reduce the subjective variance between observers. To achieve the same goal we introduced an overlap into the subsamples that are selected: we ensure that at least 10% of each subsample is also present in another subsample. In this way, a fraction of the human-viewed spectra are redshifted by two or more observers, or even by the same observer twice or more.

Using these multiply-viewed spectra we standardise the observer flags in the following way:

- For each redshifter, we examine the internal consistency of their flags. That is, if they always gave consistent flags for the same object, they will have a higher rank.
- This ranking for the redshifters will dictate which solution is accepted in the case of multiply-observed spectra.
- In addition, each observer, in order of rank, is given a shift to all flag values equal to the mean of their difference with the highest rank observer that they share > 20 objects with.
- The result of this procedure is a set of new (decimal value) flags for each object, which extends beyond 4.

In Sec. 3.2 we examine how the main results of this work change if we do not standardise the flags.

2.5 Generating the full spectroscopic sample through random forest

We use the standardised set of redshifter flags (which we will refer to as “human flags”) obtained from the previous section as a training set to expand our sample to the full spectro-

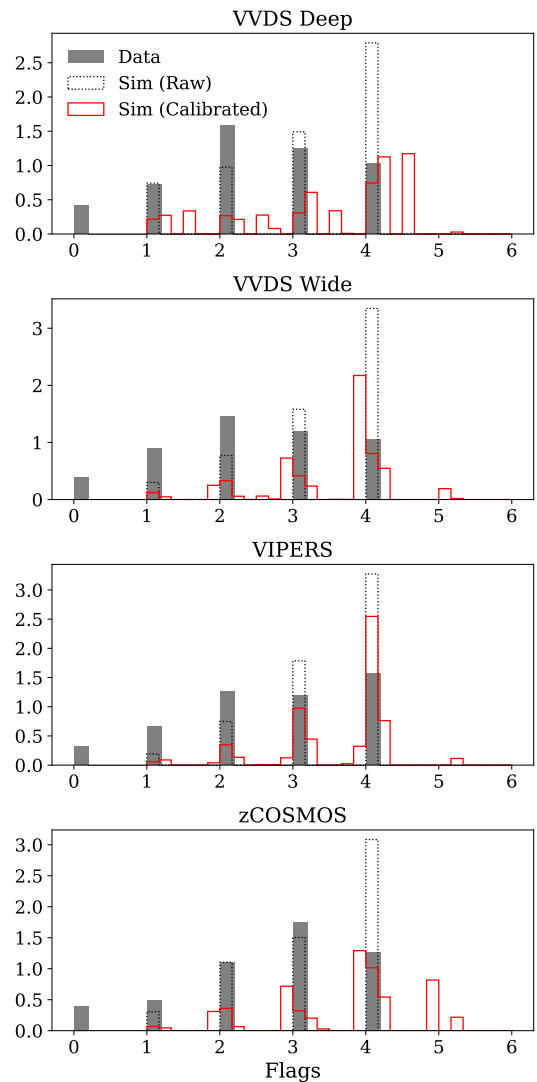


Figure 3. Distribution of human-determined redshift quality flags for our simulated datasets (dotted), compared with those from the real survey data (filled grey). We also overlay the calibrated flags in red.

scopic data set generated in Sec. 2.3. Specifically, we use a random forest (RF) in regression mode, with features computed from the simulated spectra and a single output (the redshift confidence flag).

For the training, the whole sample is used, irrespective of survey origin. The features that are used for the training are the SN of emission and absorption lines, and the strength of the 4000Å break. In particular, we calculate the S/N of the spectra in the rest-frame wavelength window $\Delta \lambda = 100 \text{ \AA}$ around the absorption lines listed in Table A1 in Appendix A.

Our approach implicitly assumes that these are the features that humans use and ignores additional information such as shape of the continuum. In practice, continuum shape is sometimes used as supporting information in a redshift determination, but it is unlikely that it is sufficient to change a moderate confidence redshift into one of high confidence.

In Fig. 2, we show RF flags for the sample where human flags are also available. We note that they are strongly correlated, but with a scatter width ~ 1 and a mean slope of the distribution that is shallower than 1. The inset panel shows a partial Receiver Operating Characteristic (ROC) curve of the RF-predicted flags, showing the completeness vs. contam-

ination of the RF sample for different threshold values of the predicted flag (Flag=2, 2.5, 3 is marked on the curve). In Sec. 3.2 we show that our results are largely insensitive to whether we use human or RF flags.

In Fig. 3 we compare the distribution of the quality flags from our simulated dataset with real distributions from VVDS, zCOSMOS and VIPERS. It is clear that our determinations are on average of higher confidence class. This is due to: 1) the fact that the simulated spectra are somewhat idealised and 2) differences between the confidence indicated by a given class between surveys – for instance, our Flag=3 corresponds more closely to Flag=2 in VIPERS. In the later analyses we investigate the redshift bias as a function of the flag limit – one could adopt a higher flag limit to account for the idealistic aspects of the simulations and any variance in the meaning of the confidence flags.

2.6 Re-weighting and the target sample

As we mentioned in Sec. 1, when using spectroscopic redshifts directly to infer the redshift distribution in weak lensing surveys, common practice is to re-weight the sample, following e.g. Lima et al. (2008), to account for any mismatch in the distributions of photometry between the spectroscopic and weak lensing data sets. We implement such a procedure, re-weighting the spectroscopic sample in our simulations (constructed by applying a given quality flag cut on the spectroscopic sample described in previous sections) to a target weak lensing sample. Weighting is performed with a *k*-nearest neighbours algorithm in four-dimensional colour-magnitude space ($g - r$, $r - i$, $i - z$, i -band magnitude), reflecting the DES survey observing strategy.

Throughout the paper, we assume four target samples – matching the four tomographic weak lensing source samples used in H18. We assign all the galaxies to four tomographic redshift bins ($0.2 < z < 0.43$, $0.43 < z < 0.63$, $0.63 < z < 0.9$, $0.9 < z < 1.3$) via the mean redshift of the $p(z)$ output by the Bayesian Photometric Redshifts code (BPZ, Benítez 2000), which is run on the simulated ‘observed’ fluxes. The BPZ set-up and binning scheme above follows the one used for the DES Y1 cosmology analysis H18. An $i < 23.4$ cut is also applied to all the four samples – this roughly mimics the weak lensing source galaxy selection, and is the target sample used throughout the paper, though real source catalogues have a softer magnitude cut due to the complexities of morphology and brightness in the selection cuts. In Table 3 we list the characteristics of this target sample compared to the DES Y1 weak lensing sample. Our target sample is slightly fainter on average than the DES Y1 sample. However, there is a tail that extends to fainter magnitudes in DES Y1 that our target sample does not include. These two contrasting differences mean that our target sample is fairly consistent with the DES Y1 sample in the mean redshift. Also note that the spectroscopic sample described previously is selected from a sub-region of this target sample.

2.7 Simplifications in our approach

Our simulations and analysis approach are idealised in several aspects. We discuss the simplifications in this section, but note that the purpose of this study is not to simulate a high-fidelity spectroscopic sample and estimate the exact value of the bias due to spectroscopic incompleteness (nor is it practical to do so). Rather, we use reasonable assumptions to illustrate the point that spectroscopic samples used to calibrate weak lensing surveys can in principle be biased due to

selection effects in constructing the spectroscopic sample itself, even after re-weighting is applied. With the simulations we can also estimate the order of magnitude of this effect and compare with other systematic uncertainties in the redshift distributions. We also note that the simplification of the simulated spectra generally leads to a conservative estimate of the bias (i.e. the true bias in the data is likely to be higher).

The first class of simplifications are those associated with simulating the spectra:

- We do not include the particularly severe red fringing that is seen in early VIMOS surveys.
- We assume fixed sky spectra and perfect knowledge of the transmission curve.
- We ignore instrument flexure, mis-aligned slit masks and poor flux calibration.
- The spectra are based on **k-correct** templates, which only produce a limited range of unique spectra.
- The Buzzard simulations themselves do not include all galaxy types as they are matched to a limited population and redshift of galaxies in SDSS.
- We specify each survey with only the parameters listed in Table 2.

The second set of simplifications and approximations are those made in the process of generating the quality flags for the full spectroscopic sample:

- We use the RF flags, which differ slightly from the flags that would be determined by a human redshifter.
- We account for the observer - observer scatter by the simple priority and standardisation scheme described in Sec. 2.4

Finally, to cleanly isolate the effect of the spectroscopic selection effects from the photometric redshift estimation algorithm:

- We use the true redshift instead of the estimated redshift when evaluating the bias in the mean redshift. Implicitly this choice also avoids the need to simulated complex survey-dependent effects such as blending, which can result in an incorrect, but confident, redshift assignment based on the wrong spectral features (e.g. (Masters et al. 2019)).

Some of the effects we neglect, e.g. poorly aligned slit masks, will produce redshift failures that are essentially random as to which objects they impact. In such cases our estimated redshift biases would not change, simply the level of shot noise in the analysis would increase if we were able to model those effects correctly. Other simplifications will have the effect of making the human redshifter’s job easier, and hence result in a more confident flag assignment. By using the canonical flag limit of $\text{Flag} \geq 3$ to determine the high-confidence sample (where appropriate) we are therefore being over-inclusive as to which objects are retained and thus under-estimating the magnitude of any redshift bias.

3 QUANTIFYING SPECTROSCOPIC INCOMPLETENESS BIAS

3.1 VIPERS: survey-constructed incompleteness

Before examining the impact of incompleteness in our simulated data, we briefly revisit sample selection effects in spectroscopic surveys. In Bonnett et al. (2016) we showed that the artificial upper redshift limit that was used for determining spectroscopic redshift solutions in the PRIMUS dataset (Cool et al. 2013) is propagated by machine learning algorithms to the redshift distribution estimation of the science

Table 3. Characteristics of the weak lensing sample in DES Y1 compared to that used in this paper with a simple magnitude cut $i < 23.4$. In this table the first number is for the DES Y1 sample and the second number the target sample used in this paper.

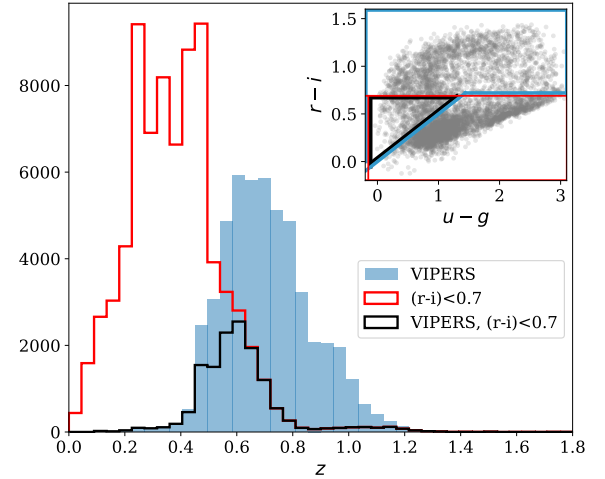
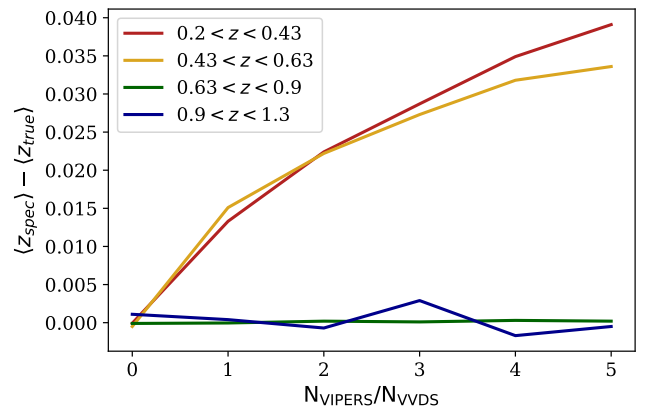
Survey	$0.2 < z < 0.43$	$0.43 < z < 0.63$	$0.63 < z < 0.9$	$0.9 < z < 1.3$
Mean magnitude	21.4; 21.7	21.7; 22.1	22.0; 22.3	22.5; 22.8
Mean redshift	0.38; 0.35	0.51; 0.45	0.74; 0.74	0.96; 0.99

sample. As a result, PRIMUS redshifts were not used in determining the redshift distributions of the weak lensing samples in DES Collaboration et al. (2016). Because of the size of the PRIMUS sample (88,040 galaxies) and the fact that this bias was imposed during redshift determination, the effect was rather clear and could not be compensated for by applying weights (e.g. Lima et al. 2008). However, spectroscopic samples are frequently selected for specific science purposes and many of the remaining samples contain biases of their own, for instance due to using colour cuts to isolate particular redshift intervals. If an employed colour cut is not available to a particular weak lensing experiment, then it is possible for small biases in redshift to be introduced during re-weighting, purely due to the projection in colour space. We demonstrate this issue using the simulated VIPERS spectroscopic sample described in Sec. 2.3 as an example. We will also for illustration purpose use a target sample that is different from what we use in the main analysis.

The VIPERS team used a pair of selection criteria in colour space to broadly separate objects at $z > 0.5$ from the lower-redshift population based on an initial i -band-selected catalogue. Identifying objects in this way enabled a very efficient survey strategy, due to strong spectral features falling within the spectral window of the LRred grism on VIMOS. The final dataset is large with high completeness (90.6% at redshift confidence $> 96\%$ ⁷, Guzzo & Vipers Team 2017) with just 45 minutes of exposure time per target. In the DES final redshift catalogue (Gschwend et al. 2018), there are similar numbers of objects from the VIPERS dataset and from the pure i -band selected sample of VVDS wide ($17.5 < i < 22.5$).

To illustrate the issue, we first apply the i -band selection criterion, $17.5 < i < 22.5$, to the Buzzard galaxy catalog. This sample will be used as the target sample here, note that the selection criteria is identical to that of VVDS wide (see Table 2). The distribution of this sample in $(r-i)$ vs. $(u-g)$ colour space is shown in the inset of Fig. 4, together with the VIPERS selection criteria (blue outline, $(r-i) > 0.5(u-g)$ or $(r-i) > 0.7$) and two other colour-defined subsamples (black and red outlines). The redshift distributions of the galaxies in these three samples are shown in the main panel of Fig. 4. As expected, the vast majority of $z > 0.5$ galaxies in the red selection region are contained within the black selection box (and hence within VIPERS), and the black region contains almost zero low-redshift galaxies. We assign all the galaxies to four tomographic redshift bins as described in Sec. 2.6.

Next, we calculate the redshift bias for a sample of galaxies that contain a mix of VIPERS and VVDS wide galaxies. The redshift bias is defined as the difference in mean redshift of the weighted spectroscopic sample and the target sample. The weighting accounts for the difference in the colour-magnitude distribution in the sample compared to the target sample, but only in the colour-magnitude space that is available to DES photometry (*griz*). Negative redshift bias values indicate the spectroscopic sample is biased towards

**Figure 4.** Redshift distribution of galaxies matching the VIPERS colour selection: $(r-i) > 0.5(u-g)$ or $(r-i) > 0.7$ (solid), an $(r-i) < 0.7$ sample and a sample selecting just where VIPERS overlaps at $(r-i) < 0.7$. These latter two samples have different redshift distributions, and so re-weighting without $(u-g)$ colour information will result in biases. **Inset:** these three samples in $(u-g)$ vs. $(r-i)$ colour space.**Figure 5.** Bias in the mean of the redshift distribution for four tomographic bins between a galaxy sample consisting a mix of VIPERS and VVDS wide galaxies and our target sample selected through a simple $17.5 < i < 22.5$ selection. A weighting scheme is applied to the redshift distribution of the galaxy sample to account for the difference in the colour-magnitude distribution in the VIPERS/VVDS sample and the target sample. From left to right, we vary the relative fraction of VIPERS and VVDS galaxies. The mean redshift is biased high in the two lower redshift bins when a significant fraction of the sample comes from VIPERS.

⁷ This estimate includes slightly lower confidence flags than typically used for weak lensing analyses.

low redshift. Fig. 5 gives the bias in each tomographic bin where the target sample is always the full sample with the $17.5 < i < 22.5$ magnitude selection. The x-axis corresponds to different ratios in the number of VIPERS sources to VVDS wide sources. The samples are assumed 100% complete and occupy the same region of sky – hence the bias is due purely to the imprint of the VIPERS colour selection function.

We note here that when only VVDS wide galaxies are used ($N_{\text{VIPERS}}/N_{\text{VVDS}} = 0$), the spectroscopic sample is just a subset of the target sample, therefore the reweighting is perfect and the bias is essentially zero.

However, as we move to the right on the x-axis in Fig. 5, we see that the two low redshift bins become more biased as the fraction of VIPERS galaxies increase in the sample – the bias is around a couple of per cent and increases the mean redshift of the bin. This is due to the lack of low redshift VIPERS galaxies that did not get properly compensated with the weighting scheme. On the other hand, the biases in the high redshift bins are much smaller and consistent with being simple noise fluctuations. In DES Y1 data, $N_{\text{VIPERS}}/N_{\text{VVDS}} \sim 1$, suggesting a ~ 0.015 bias in the mean redshift in the low redshift bins. One way to think of this selection function is that relative to a complete $17.5 < i < 22.5$ sample, the spectroscopic data set is systematically incomplete at red $u - g$ colours and blue $r - i$ colours. The crucial point here is that information is used to select objects that is not accessible to the survey, and hence the selection cannot be compensated for.

There is similar potential for a selection-induced bias in relying heavily on the DEEP2 data set. The DEEP2 team used a set of softened colour cuts to pre-select galaxies at $z > 0.75$ in three of their four fields, including the one covered by DES data. These colour cuts used B, R and I-band data, and therefore cannot be reproduced in the DES photometry.

We can draw a direct analogy from the VIPERS example above to generic selections of spectroscopic samples – it is the strength of the available spectral features that determine whether a galaxy can be used for redshift validation. These spectral features are similarly information used for the selection that cannot be accessed with the photometric survey data. We will now examine the impact of making selections on spectroscopic information.

3.2 Impact of incompleteness

Having examined the simple case in Sec. 3.1, we now move on to the full spectroscopic sample constructed in Sec. 2. We combine the four simulated surveys as is typically done with real data: naively concatenating the data sets, cutting galaxies below some redshift flag criterion and then giving each object a weight such that the overall sample mimics the colour-magnitude distribution of the target sample (here, we weight in *griz*, as done in DES Y1). We then compute the difference in mean redshift between this incomplete sample and the target sample (four $i < 23.4$ magnitude-limited tomographic bins at $0.2 < z < 0.43$, $0.43 < z < 0.63$, $0.63 < z < 0.9$, $0.9 < z < 1.3$), using the true redshifts of the simulated galaxies – i.e. we assume that human redshift determinations are infallible. In our data this was indeed the case for the higher quality redshifts (Flag ≥ 3), but is in general not the case, even for the highest confidence objects. For instance, blends of multiple objects at different redshifts lead to ambiguities, or even assigning a fairly bright galaxy the redshift of a much fainter one due to only one of the galaxies exhibiting emission lines (Masters et al. 2019). The spectroscopic sam-

ple is re-weighted as described in Sec. 2.6 and an estimate of the redshift distribution for the target sample is derived.

Fig. 6 shows the completeness and $\langle z_{\text{spec}} \rangle - \langle z_{\text{true}} \rangle$ as a function of the flag limit. Here $\langle z_{\text{spec}} \rangle$ is the mean redshift for the unweighted and weighted spectroscopic sample after some flag limit selection and $\langle z_{\text{true}} \rangle$ is the mean redshift of the target sample. We use a simple $i < 23.4$ target sample and the tomographic redshift bins as described in Sec. 2.6. The target sample in Fig. 6 covers the same fields as the spectroscopic survey. This is not to say that it is entirely free from sample variance effects, and in fact $\langle z_{\text{spec}} \rangle - \langle z_{\text{true}} \rangle$ is nonzero even when objects with very poor flags are included in the spectroscopic sample (Flag ~ 1). After weighting, however, $\langle z_{\text{spec}} \rangle - \langle z_{\text{true}} \rangle$ is reduced to < 0.01 across all tomographic bins. Raising the flag limit we begin to see a degradation in mean redshift recovery with respect to the complete sample case, even after weighting. At a nominal high-confidence cut, Flag ≥ 3 , the bias is still small ($< 0.01 - 0.02$) in the three lower-redshift bins; though we note that this level of error is already barely within the target accuracy. The highest redshift bin suffers a substantial bias of ~ 0.05 . An error of this size means that incomplete spectroscopic samples such as those considered here are a poor choice for validating high-redshift samples. We show in Fig. 7 redshift histograms for the samples cut at confidence Flag ≥ 3 . Visually, we see that the reweighting scheme performs well in recovering the shape of the redshift distributions in all bins, correcting differences in the tails as well as the shape of the core distribution. However, there are some small differences remaining, resulting in the overall error in the mean redshift.

The fact that the effect of spectroscopic incompleteness is most severe in the high redshift tomographic interval is hardly a surprise. The range $0.9 < z < 1.3$ includes galaxies with important strong spectral features – the 4000Å break and [OII] emission line doublet – buried in bright sky lines or even falling outside the useful spectral window of the red VIMOS grisms. Galaxies at these redshifts are also fainter on average than those in the lower redshift subsamples, and the increased photometric errors act to broaden the redshift distribution at any given location in colour space. The combination of redshift-dependent incompleteness at fixed colour and reduced ability to localise objects in colour-magnitude space results in weighting being ineffective.

As noted above, the y-axis in the bottom panel of Fig. 6 (lower panel) contains both the effect from the flag limit cut and the fact that there is field-to-field variance between the four spectroscopic surveys we are simulating. In Appendix B we isolate the two effects and show that our main conclusions remain the same.

We have also tested the full analysis using unstandardised (integer) flags and show the results as diamond markers in Fig. 6 and Fig. B1. Overall the predicted biases are lower with unstandardised flags and look visually more similar to the human flags described later in Sec. 3.3. However, we decide to use the RF flag in our fiducial analysis because 1) the flags in real data are not always integers and 2) the flag assignment (and therefore the exact structure in the curves in Fig. 6) is arbitrary and survey-dependent. In addition, since the bias in the highest redshift bin with the unstandardised flags still exceeds the requirement, our main conclusion does not change qualitatively. Essentially we can view the standardised and unstandardised flags to bracket the range of biases we expect.

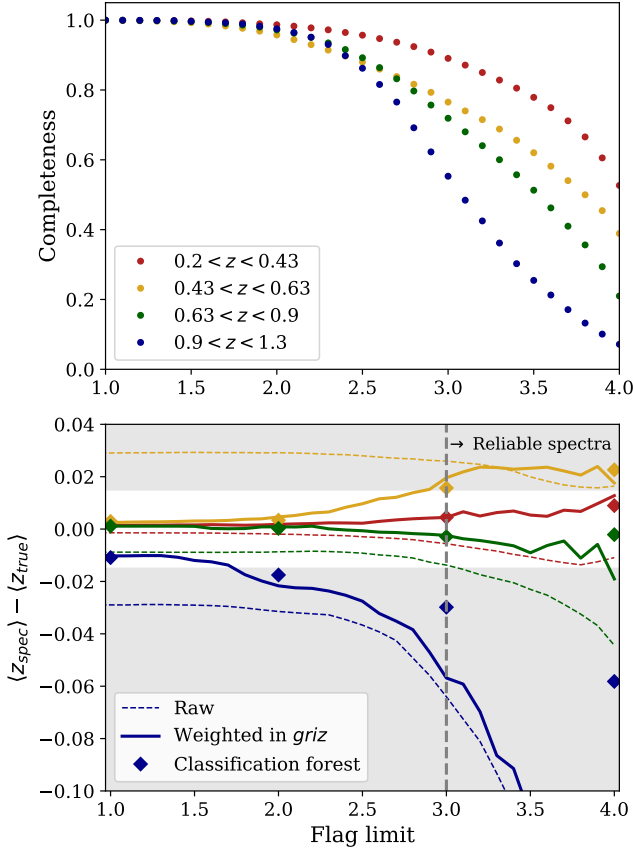


Figure 6. **Upper panel:** Survey completeness as a function of flag limit in each tomographic redshift interval, split using the mean redshift derived by BPZ, as performed in the main DES analysis. **Lower panel:** Bias in mean weighted redshift as a function of flag limit. The spectroscopic sample is weighted to match the colour-magnitude space of a sample complete to $i < 23.4$ in the same simulation fields. The bias in the mean redshift comes from systematic incompleteness in the spectroscopic sample. The diamond markers show the same results using unstandardised flags. We also highlight the region $|\delta z| < 0.015$, which is the approximate uncertainty in the DES Y1 photo- z from COSMOS15 calibration.

3.3 Dependence of target and comparison with human flags

Previously, we have assumed that our weak lensing source sample, or the target sample, is a $i < 23.4$ magnitude-limited sample. We also noted in Table 3 that this target sample is slightly deeper than the DES Y1 weak lensing sample. Here we explore a more general situation and ask how our results change when we vary the magnitude limit of the sample. Effectively this shows, with the same spectroscopic sample, the change in the redshift bias from spectroscopic incompleteness as a function of the survey depth. The left panels of Fig. 8 show the redshift biases for the raw and weighted samples at different depths, for the highest source bin in Fig. 6. As expected, the bias becomes greater as we go to deeper target samples. While the reweighting can correct for some of the incompleteness, once the target sample is deeper than $i \sim 23$, the limitation of the reweighting becomes apparent, as the number of spectra at those depths become relatively sparse as well.

We also show, in the right panels of Fig. 8, the same plot as the left panels, but using human redshift flags instead of the RF flags. There are several characteristics of this plot which are different from the left panels that come from the

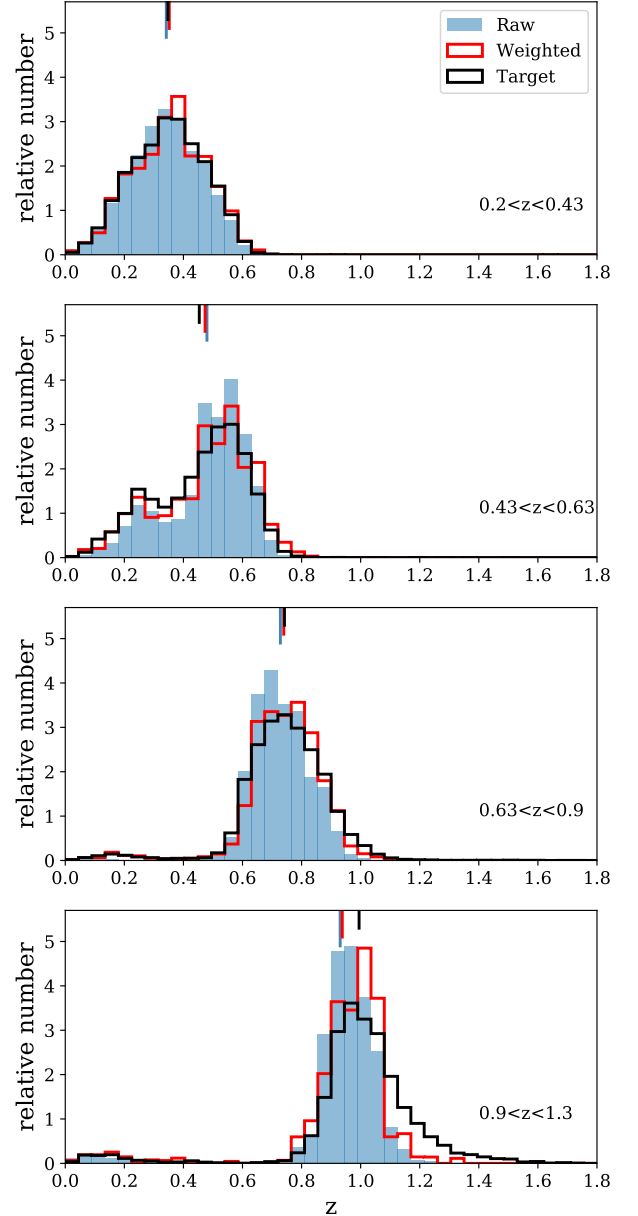


Figure 7. Redshift histograms for complete (black), incomplete at $\text{Flag} < 3$ (blue shaded) and weighted (red) samples. The weighting matches the incomplete sample to the complete one in colour-magnitude space, but results in residual mismatches in the redshift distribution. The bars on the top of each panel mark the mean redshift for each of the distributions.

construction of two sets of flags: First, the human flags are much fewer in number and therefore noisier. Second, the human flags are more quantised, which is expected since the human flags cluster more around integers and the RF flags smooth out this behavior. Third, the rolloff of the curves going from flag 3 to flag 4 in the RF flags seem a lot faster than the human flags. This could be the RF interpolating over regions without a lot of data. Fourth, there is one curve ($i \sim 23.2$) in the human flags that appears qualitatively different from the others; this is likely due to noise.

We note that, despite these differences, our main conclusion holds for both human and RF flags: at the relevant flag limits of 3-3.5, the redshift bias in a DES Y1-like weak lensing sample at redshift > 0.9 exceeds the uncertainty in other calibration methods. These results are consistent with

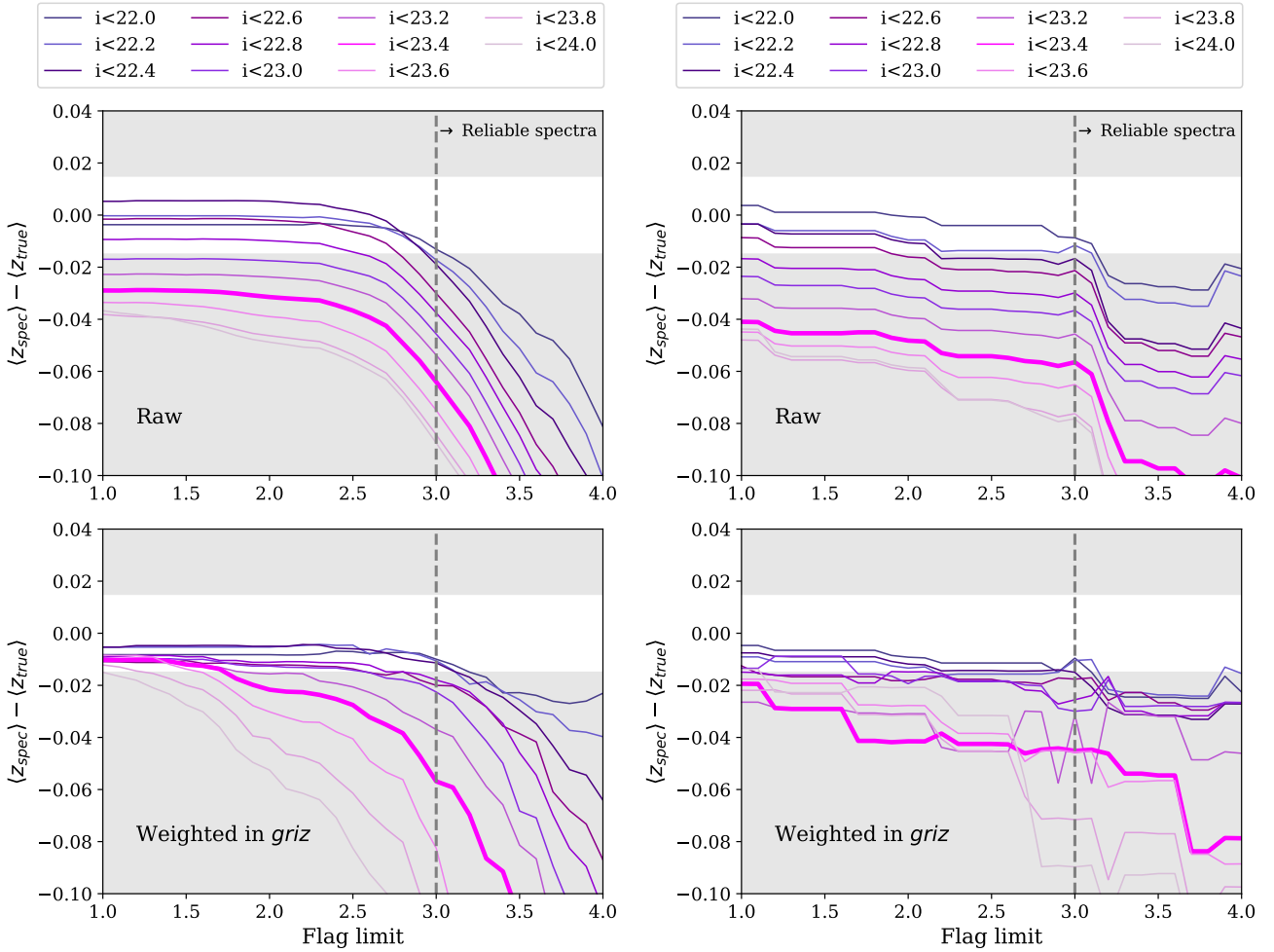


Figure 8. **Left panels:** Redshift bias from spectroscopic incompleteness as a function of flag limits for target samples of different depth, at $0.9 < z < 1.3$. The upper panel shows the bias from the raw sample while the lower panel shows the bias in the reweighted sample. We highlight the region $|\delta z| < 0.015$, which is the approximate uncertainty in the DES Y1 photo- z from COSMOS15 calibration. We also mark flag limit = 3, which is the typical flag limit adopted to construct spectroscopic samples. **Right panels:** Same as the left panel but only using human redshift flags and not RF flags. In both panels, the thick lines mark the fiducial target sample used in this work.

that shown in Bonnett et al. (2016) and Gruen & Brimiouille (2017). The former estimated a bias of 0.05 for the DES Science Verification dataset, while the latter measured the bias in the mean redshift introduced from spectroscopic incompleteness in existing data to be at the level of ~ 0.1 with a much deeper sample $i < 25$. In Appendix C we compare our results with those estimated by Gruen & Brimiouille (2017) for a sample matched in limiting i -band magnitude.

3.4 Discussion

The effect that we have investigated can be summarised as a deficit in our knowledge of $p(z, T, \mathbf{flux})$. Here, \mathbf{flux} represents the vector of photometry measurements to be used, and clearly correlates with redshift, z , and galaxy SED type, T . Through spectroscopy we have access to only a limited region of this joint probability space of redshift, galaxy SED and flux, while in our target sample we know just the marginal distribution, $p(\mathbf{flux})$. Even in the best cases, e.g. upon completion of the C3R2 programme (Masters et al. 2017), we will still have a selection function in \mathbf{flux} with respect to the target sample - i.e. there is a covariate shift. In the samples used in this work this selection function is in both brightness and colour, while in a completed C3R2 it would be in brightness

alone. Because $p(\mathbf{flux})$ correlates with z and T in a way that is currently unknowable accurately, matching the marginal distributions in $p(\mathbf{flux})$ of the spectroscopic and target samples cannot guarantee the correct recovery of $p(z, T, \mathbf{flux})$, or the marginal $p(z)$. In other words, multiple different distributions in $p(z, T, \mathbf{flux})$ can result in the same marginal distribution, $p(\mathbf{flux})$, and without full knowledge of $p(z, T)$ we are blind to which of them is correct. In practice the situation is likely to be worse than this, and even the eventual C3R2 will likely suffer some degree of (unknown) selection in z and T in addition to \mathbf{flux} . In order to use a simple weighted spectroscopic sample as an estimator of the redshift distribution of a weak lensing sample we therefore require a sample complete in both colour and amplitude (i.e. \mathbf{flux}), with very low incompleteness of targeted objects.

In the case that the spectroscopic samples are not complete (or at least very close to complete) and that failures are not random in redshift, then the fundamental problem that we demonstrate in this paper is formally undefined and therefore cannot be solved. There is no solution that is identifiable in a statistical sense, in that we cannot use the data available to correct for the missing objects. To be clear, we do not know *a priori* that a given incomplete spectroscopic sample is inadequate and will introduce a bias, but without

filling in the missing data neither can we be confident that we are free of important biases.

While we have explored a very simple algorithm for estimating weak lensing redshift distributions from a spectroscopic sample, the issue of non-identifiability extends to almost all approaches of inferring redshift distributions (one notable exception perhaps being the use of cross-correlation with a reference redshift sample, e.g. Newman 2008). For instance, in deriving redshift probabilities via model fitting, we cannot be confident that our SED set is complete if we do not have a complete spectroscopic sample to test them against. Similarly, more sophisticated algorithms that attempt to separate the colour-redshift likelihood from the population density, such as Self Organising Maps (SOMs), may have greater robustness to incompleteness but cannot solve the underlying issue entirely. All we can hope to achieve is to reduce the uncertainties introduced to an acceptable level for a given cosmological analysis. In the next section we introduce a number of possible ways to approach that task.

4 MITIGATION APPROACHES

We established in the previous section that spectroscopic incompleteness could introduce a bias in the mean redshift for tomographic weak lensing samples. Here we discuss three potential approaches to mitigate such biases. First, we consider using lower confidence flags for selection of spectroscopic samples (Sec. 4.1). Second, we consider removing particular regions in colour-magnitude space where the spectra are affected seriously by incompleteness (Sec. 4.2). Third, we consider correcting such biases via simulations (Sec. 4.3).

4.1 Using lower-confidence redshifts

Incompleteness in spectroscopic samples is not only a challenge for cosmology experiments. The key surveys we have been simulating were originally designed to answer questions about the evolution of galaxies and incompleteness can bias those answers just as it can bias cosmological parameter estimation. In Lilly et al. (2009) it was suggested that the confidence in a spectroscopic redshift could be increased if it is later found to agree with a precise photometric redshift (such as are available in the COSMOS field), because the photometric redshift uses complementary information. In this way, they proposed a statistically complete sample which supplemented the high-confidence redshifts with objects that showed just such agreement.

From Fig. 6, it is clear that using objects with confidence flags as low as 2 would achieve a level of bias close to the precision quoted in H18, but would be insufficient for the highest tomographic bin in any future analysis. We would need to use essentially all galaxies in the sample for spectroscopy to be a useful addition to the validation process. It is not obvious that all low-confidence objects will match their respective high-quality photo- z , and the worry that some of these are nevertheless wrong is a concern. Our simulations are not realistic enough to assess this final point and we leave it to future work, using more sophisticated simulations, to explore.

4.2 Removing troublesome regions of colour-magnitude space

When probing the large-scale structure, one of the main differences between using weak lensing and using galaxy densities is that for weak lensing the galaxy sample used for shear

measurements does not need to be complete, since they are merely probes of the lensing field. That is, we could attempt to trade statistical precision (i.e. use fewer galaxies) to reduce biases caused by systematic errors in the galaxy sample, such as the effect studied in this paper – incompleteness of the spectroscopic samples. A natural approach is to use galaxy photometry to isolate subsets of our sample that are likely to be impacted by biases due to incompleteness and exclude them from the weak lensing sample. We investigate here one approach for doing this – using Self-Organising Maps (SOM, Kohonen 1982). An SOM maps a high-dimensional space into lower dimensionality (typically 2-D) via an artificial neural network; SOMs were introduced as a tool for exploring colour-space coverage of spectroscopic data sets in cosmology by Masters et al. (2015). An SOM enables one to cleanly assign each galaxy to a subsample in the quantised photometric space.

We construct our SOM using $g - r$, $r - i$, $i - z$ and i -band magnitude from the $i < 23.4$ simulated photometric data. We choose a 28×28 square map, with $\sigma = 3$, learning rate = 0.4 and periodic boundaries, using the python package *MiniSom*⁸. We have confirmed that our conclusions are insensitive to reducing the map size and to the precise values of the hyperparameters. However for this simple exploration we have not attempted to optimise the SOM parameters. For each cell in the SOM, we collect the spectroscopic redshifts of the galaxies that belong to that cell and determine whether to retain or discard that cell based on a simple metric. We perform two runs, once with each of the following criteria:

- If the spectroscopic failure rate is above f_{fail} (we use $\text{Flag} < 3$ as a criteria for a failed redshift)
- If the intrinsic true redshift dispersion in the cell is greater than σ_{spec}

After discarding certain SOM cells in both the spectroscopic sample and the weak lensing sample, we reweight the spectroscopic galaxies to match the weak lensing sample in the same way as described in Sec. 2.6. We then explore how the bias due to spectroscopic incompleteness changes as we removed progressively more cells from the analysis.

Fig. 9 shows the bias in each redshift bin as a function of the fraction of the $i < 23.4$ photometric sample that is retained for the case where the two different criteria were used to discard SOM cells. We have also explored the extreme case of the effect, using the $i < 24$ sample, to determine whether it is a suitable approach that could be used for the final DES data set. Our conclusions are unaltered with respect to the $i < 23.4$ sample, but reflect the larger bias seen in Fig. 8. The uncertainties were derived by 50 realisations of the SOM random seed, and therefore represent the uncertainty in the SOM method only.

It is clear from Fig. 9 that redshift dispersion is the more effective indicator to use for overcoming biases from spectroscopic incompleteness. However, to reduce the impact to a similar level of uncertainty as H18 we must remove on the order of two thirds of our highest redshift bin. Therefore, while it is a possible mitigation strategy, this seems impractical for use in DES – the degradation of statistical power will have a much larger impact than simply marginalising over a few percent of redshift biases from the spectroscopic incompleteness. Note, however, that as we reduce statistical precision, the impact of photo- z biases in the final parameter constraints will become less important. With poorer statistical power we would be able to allow a greater error budget

⁸ <https://github.com/JustGlowing/minisom>

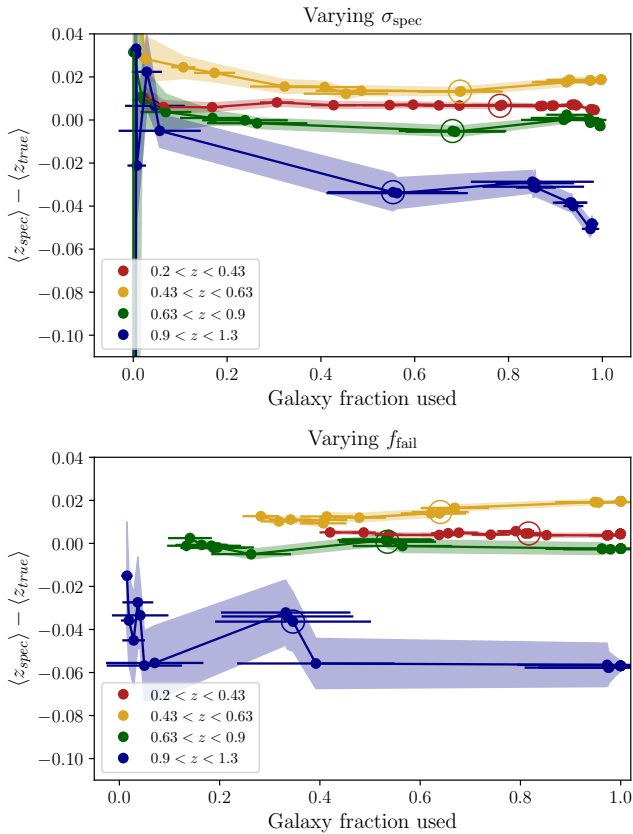


Figure 9. Redshift bias from spectroscopic incompleteness in the four weak lensing tomographic bins as a function of the fraction of source galaxies used. All values here are after reweighting has been applied. From right to left, we remove increasingly more cells from an SOM quantisation of the colour-magnitude space. The removal of cells for the upper (lower) panel is based on the intrinsic spectroscopic redshift scatter σ_{spec} (fraction of galaxies where we failed to get a high-confidence redshift f_{fail}). Large open circles mark $\sigma_{\text{spec}} = 0.2$ (upper panel) and $f_{\text{fail}} = 0.5$ (lower panel), the mid points of the ranges we consider.

in the redshift distributions and could therefore optimise the sample with somewhat greater numbers than Fig. 9 suggests.

This is not to say that approaches aiming to reduce incompleteness-related biases with SOMs are necessarily futile. At higher dimensionality (e.g. KiDS+VIKING, Euclid+EXT, DES+VIDEO) they may see greater success, as the SOM cells will have narrower intrinsic redshift dispersion (provided photometric uncertainties are not large). Moreover, implementations with greater sophistication than the fairly naive one used in this work (e.g. Alarcon et al. 2019; Buchs et al. 2019; Sánchez & Bernstein 2019; Wright et al. 2019) could be capable of more promising results. Most of these methods seek to gain an advantage by also utilising higher-dimensional data. However, these are clearly areas of development work that are beyond the scope of this paper.

4.3 Using simulation results to correct biases in real samples

It is tempting to ask whether we could simply use the bias computed from our simulations (or a more sophisticated version of them) to correct the mean redshift of real spectroscopic data sets, and thereby be able to use spectroscopy to validate the redshift distributions in weak lensing experiments. It could be worth further investigation, but it would

be extremely challenging in the short term. To accurately simulate the bias directly we would need to know the true galaxy distribution in redshift and SED type, have accurate galaxy SEDs and be able to select a target weak lensing sample from the simulations that represents the true target sample. Clearly, if we were confident that we had all of this information then our problem is already solved and we would have no need to perform these simulations.

One could instead imagine deriving galaxy type and redshift-dependent incompleteness factors, which removes the need for an a priori correct redshift distribution or mix of galaxy types. As the redshift confidence flag depends on feature strength in the spectra, we would still need to be confident that the equivalent widths of emission and absorption lines in our simulations are appropriate at any given redshift. Though our knowledge of high-redshift galaxy spectra and SEDs has increased greatly over recent years (e.g. Maltby et al. 2016; Wuyts et al. 2016; Kashino et al. 2017; Forrest et al. 2018), we are still not quite at that stage.

5 SUMMARY

One of the crucial components for weak lensing as a cosmological probe is the redshift distribution of the source galaxy sample. Even small biases in the estimated redshift distributions can lead to important biases in the final cosmological parameter estimates. These potential biases in redshift, and the methods to overcome them or incorporate them in analyses via nuisance parameters, have been the focus of a growing literature (e.g. Cunha et al. 2012; Masters et al. 2015; Bonnett et al. 2016; Gruen & Brimiouille 2017; Hoyle et al. 2018; Joudaki et al. 2019). In this work, we examine one particular method in which the redshift distributions are obtained – by directly weighting the redshifts of a spectroscopic sample based on the photometric properties of the spectroscopic sample and the weak lensing source galaxies. In an idealised situation where the following is true, this method results in an unbiased estimate of the redshift distribution up to the limit of sample variance:

- The spectroscopic redshifts of the sample being weighted are all correct.
- The uncertainties in the photometry of the spectroscopic sample are representative of the target sample.
- At any given locale in photometric space, the available spectroscopic redshifts are equivalent to a random draw from the true redshift distribution of the target sample in that same locale.

We examine the validity of the last assumption here through the use of simulated spectroscopic surveys, ensuring the other two conditions are met by construction. In particular, we investigate how the spectroscopic samples that are assembled for this purpose are typically incomplete due to the “redshifting” procedure – human observers inspecting each spectrum and assigning confidence flags to indicate how secure the determined redshift is. As only highly-confident redshifts can be used, this process introduces a subtle selection effect. Spectra of certain types and redshifts are preferentially given a lower flag values due to having fewer or less prominent features such as spectral lines or breaks. These features are not uniquely determinable from the broad band photometry available to weak lensing experiments, and could lead to a redshift-dependent success rate in determining a confident redshift at fixed locale in colour-magnitude space. In this way, an incompleteness in the spectroscopic sample

could lead to a different inferred mean redshift of the target sample compared to the case of having a complete spectroscopic sample. This incompleteness-related bias from the spectroscopic sample cannot be removed with the commonly-employed re-weighting procedure of Lima et al. (2008).

We carry out a simulated analysis to estimate the order of magnitude of this source of bias for a dataset similar to the first year weak lensing analysis from the Dark Energy Survey (DES). Simulated spectra (which include simple noise and sky models) are constructed to match three of the four key spectroscopic surveys covered by DES and passed to experienced observers, or “redshifters”, to assign quality flags. Using these human-redshifted spectra as a training set, we use a random forest approach to enlarge the sample of spectra to a similar sample size as that available to be used in DES Y1. Next, we derive the re-weighted redshift distributions for the DES Y1-like weak lensing sample and compare the mean redshift of these distributions to that of the true redshift distribution. We find that at a conservative redshift flag limit, $\text{Flag} \geq 3$, the incompleteness-induced biases, $z_{\text{spec}} - z_{\text{true}}$, in mean redshift are 0.004, 0.020, -0.002 and -0.057 for our four tomographic bins ($0.2 < z < 0.43$, $0.43 < z < 0.63$, $0.63 < z < 0.9$ and $0.9 < z < 1.3$, respectively). Using only human-redshifted objects, these become 0.005, 0.018, -0.003 and -0.045 respectively.

We further explore how the bias in the highest tomographic bin depends on the magnitude limit of the target sample, finding that it becomes rapidly and progressively worse at depths greater than DES-Y1. In two of our bins, these biases are at a similar or larger level than the uncertainties of the photometric redshift derived from COSMOS15, suggesting that direct re-weighting of the spectroscopic redshifts is not an appropriate approach for DES Y1, nor for the future DES analyses that will require still greater accuracy.

The impact of incompleteness is likely to be most severe for surveys in which the intrinsic redshift distribution is broad in at least part of the photometric space (either due to low dimensionality or significant photometric errors), and where the target sample extends to redshifts that are challenging to recover with current high-multiplex spectrographs – the so-called “redshift desert”. Stage IV weak lensing experiments such as Euclid and LSST are therefore likely to face great difficulties in using spectroscopic redshifts for direct validation, not withstanding tremendous efforts such as the C3R2 programme (Masters et al. 2017, 2019).

It is worth noting that spectroscopic incompleteness is not only problematic for direct calibration of photometric redshift distributions. Template SEDs used in deriving individual galaxy PDFs are either drawn from low-redshift data, where obtaining a representative sample to low luminosity is possible, or synthetic composite SEDs build up from stellar isochrones. To be useful at the accuracy required from cosmology analyses, these SEDs and their associated prior probabilities need to be calibrated across the redshift range that will be used or, perhaps, jointly estimated along with photometric redshifts (Leistedt et al. 2019). Spectroscopic redshifts are frequently used for this purpose (though low dispersion spectra or precise photometric redshift might also be used, Forrest et al. 2018; Hoyle et al. 2018). Redshift-dependent selection effects may therefore subtly distort the calibrations applied, with the risk that these distortions too introduce redshift biases.

There are, however, potential ways one could remove the redshift biases introduced in a DIR-like method by incomplete spectroscopic samples. We showed in Sec. 4.2 that the bias due to incompleteness could be substantially reduced by

excluding regions of photometric space from a weak lensing analysis, but at the cost of removing 60 – 70% of the target sample in the highest redshift interval. The situation could greatly improve if a larger number of bands were available. Amongst the current methods being developed to deliver robust redshift distributions, perhaps the most encouraging are the combination of photometric and clustering information (Alarcon et al. 2019; Rau et al. 2019) or methods of inferring the intrinsic galaxy population by forward modelling the entire survey transfer function onto simulated observed skies (Herbel et al. 2017; Fagioli et al. 2018).

Finally, we note that there are a number of simplifications that were used in this analysis (as summarised in Sec. 2.7) as accounting for all the details of the different spectroscopic samples in the simulations is prohibitively impractical. Our approach likely produces more idealised spectra and thus a conservative estimate of the bias in redshift. We expect the true incompleteness in spectroscopic samples is equal to or worse than that which we have found, which implies a systematic uncertainty larger than what can be tolerated in present and future lensing surveys.

ACKNOWLEDGEMENT

We thank Andrina Nicola for early consultant on spectra simulations. CC is supported by the Henry Luce Foundation.

Funding for the DES Projects has been provided by the U.S. Department of Energy, the U.S. National Science Foundation, the Ministry of Science and Education of Spain, the Science and Technology Facilities Council of the United Kingdom, the Higher Education Funding Council for England, the National Center for Supercomputing Applications at the University of Illinois at Urbana-Champaign, the Kavli Institute of Cosmological Physics at the University of Chicago, the Center for Cosmology and Astro-Particle Physics at the Ohio State University, the Mitchell Institute for Fundamental Physics and Astronomy at Texas A&M University, Financiadora de Estudos e Projetos, Fundação Carlos Chagas Filho de Amparo à Pesquisa do Estado do Rio de Janeiro, Conselho Nacional de Desenvolvimento Científico e Tecnológico and the Ministério da Ciência, Tecnologia e Inovação, the Deutsche Forschungsgemeinschaft and the Collaborating Institutions in the Dark Energy Survey.

The Collaborating Institutions are Argonne National Laboratory, the University of California at Santa Cruz, the University of Cambridge, Centro de Investigaciones Energéticas, Medioambientales y Tecnológicas-Madrid, the University of Chicago, University College London, the DES-Brazil Consortium, the University of Edinburgh, the Eidgenössische Technische Hochschule (ETH) Zürich, Fermi National Accelerator Laboratory, the University of Illinois at Urbana-Champaign, the Institut de Ciències de l’Espai (IEEC/CSIC), the Institut de Física d’Altes Energies, Lawrence Berkeley National Laboratory, the Ludwig-Maximilians Universität München and the associated Excellence Cluster Universe, the University of Michigan, the National Optical Astronomy Observatory, the University of Nottingham, The Ohio State University, the University of Pennsylvania, the University of Portsmouth, SLAC National Accelerator Laboratory, Stanford University, the University of Sussex, Texas A&M University, and the OzDES Membership Consortium.

Based in part on observations at Cerro Tololo Inter-American Observatory, National Optical Astronomy Observatory, which is operated by the Association of Universi-

ties for Research in Astronomy (AURA) under a cooperative agreement with the National Science Foundation.

The DES data management system is supported by the National Science Foundation under Grant Numbers AST-1138766 and AST-1536171. The DES participants from Spanish institutions are partially supported by MINECO under grants AYA2015-71825, ESP2015-66861, FPA2015-68048, SEV-2016-0588, SEV-2016-0597, and MDM-2015-0509, some of which include ERDF funds from the European Union. IFAE is partially funded by the CERCA program of the Generalitat de Catalunya. Research leading to these results has received funding from the European Research Council under the European Union's Seventh Framework Program (FP7/2007-2013) including ERC grant agreements 240672, 291329, and 306478. We acknowledge support from the Brazilian Instituto Nacional de Ciência e Tecnologia (INCT) e-Universe (CNPq grant 465376/2014-2).

This manuscript has been authored by Fermi Research Alliance, LLC under Contract No. DE-AC02-07CH11359 with the U.S. Department of Energy, Office of Science, Office of High Energy Physics.

REFERENCES

- Aihara, H., Armstrong, R., Bickerton, S., et al., 2017, ArXiv e-prints, arXiv:1702.08449
- Alarcon, A., Sánchez, C., Bernstein, G. M., Gaztañaga, E., 2019, arXiv e-prints, arXiv:1910.07127, arXiv:1910.07127
- Albrecht, A., Bernstein, G., Cahn, R., et al., 2006, ArXiv Astrophysics e-prints: astro-ph/0609591, arXiv:astro-ph/0609591
- Asgari, M., Tröster, T., Heymans, C., et al., 2019, arXiv e-prints, arXiv:1910.05336, arXiv:1910.05336
- Bender, R., Appenzeller, I., Böhm, A., et al., 2001, in *Deep Fields*, edited by Cristiani, S., Renzini, A., Williams, R. E., 96
- Benítez, N., 2000, ApJ, 536, 571, astro-ph/9811189
- Benjamin, J., Van Waerbeke, L., Heymans, C., et al., 2013, MNRAS, 431, 2, 1547, arXiv:1212.3327
- Bielby, R., Hudelot, P., McCracken, H. J., et al., 2012, A&A, 545, A23, arXiv:1111.6997
- Bonnett, C., Troxel, M. A., Hartley, W., et al., 2016, Phys.Rev.D, 94, 4, 042005, arXiv:1507.05909
- Brammer, G. B., van Dokkum, P. G., Franx, M., et al., 2012, ApJS, 200, 2, 13, arXiv:1204.2829
- Buchs, R., Davis, C., Gruen, D., et al., 2019, MNRAS, 489, 1, 820
- Childress, M. J., Lidman, C., Davis, T. M., et al., 2017, MNRAS, 472, 1, 273, arXiv:1708.04526
- Choi, A., Heymans, C., Blake, C., et al., 2016, MNRAS, 463, 4, 3737, arXiv:1512.03626
- Cool, R. J., Moustakas, J., Blanton, M. R., et al., 2013, ApJ, 767, 2, 118, arXiv:1303.2672
- Cooper, M. C., 2006, in *American Astronomical Society Meeting Abstracts*, vol. 38 of *Bulletin of the American Astronomical Society*, 1159
- Cooper, M. C., Yan, R., Dickinson, M., et al., 2012, MNRAS, 425, 3, 2116, arXiv:1112.0312
- Crocce, M., Pueblas, S., Scoccimarro, R., 2006, MNRAS, 373, 369, astro-ph/0606505
- Cunha, C. E., Huterer, D., Busha, M. T., Wechsler, R. H., 2012, MNRAS, 423, 909, arXiv:1109.5691
- Cunha, C. E., Huterer, D., Lin, H., Busha, M. T., Wechsler, R. H., 2014, MNRAS, 444, 1, 129, arXiv:1207.3347
- Dawson, K. S., Kneib, J.-P., Percival, W. J., et al., 2016, AJ, 151, 2, 44, arXiv:1508.04473
- de Jong, J. T. A., Verdoes Kleijn, G. A., Boxhoorn, D. R., et al., 2015, A&A, 582, A62, arXiv:1507.00742
- De Vicente, J., Sánchez, E., Sevilla-Noarbe, I., 2016, MNRAS, 459, 3, 3078, arXiv:1511.07623
- DeRose, J., Wechsler, R. H., Becker, M. R., et al., 2019, arXiv e-prints, arXiv:1901.02401, arXiv:1901.02401
- DES Collaboration, Abbott, T., Abdalla, F. B., et al., 2016, Phys.Rev.D, 94, 2, 022001, arXiv:1507.05552
- DES Collaboration, Abbott, T. M. C., Abdalla, F. B., et al., 2019, Phys.Rev.D, 99, 12, 123505
- Faber, S. M., Phillips, A. C., Kibrick, R. I., et al., 2003, The DEIMOS spectrograph for the Keck II Telescope: integration and testing, vol. 4841 of *Society of Photo-Optical Instrumentation Engineers (SPIE) Conference Series*, 1657–1669
- Fagioli, M., Riebertsch, J., Nicola, A., et al., 2018, JCAP, 2018, 11, 015, arXiv:1803.06343
- Flaugher, B., Diehl, H. T., Honscheid, K., et al., 2015, AJ, 150, 150, arXiv:1504.02900
- Forrest, B., Tran, K.-V. H., Broussard, A., et al., 2018, ApJ, 863, 2, 131, arXiv:1807.03785
- Garilli, B., Fumana, M., Franzetti, P., et al., 2010, Publ. Astron. Soc. Pac., 122, 827, arXiv:1005.2825
- Garilli, B., Guzzo, L., Scoddeggio, M., et al., 2014, A&A, 562, A23, arXiv:1310.1008
- Garilli, B., Le Fèvre, O., Guzzo, L., et al., 2008, A&A, 486, 3, 683, arXiv:0804.4568
- Gruen, D., Brimiouille, F., 2017, MNRAS, 468, 1, 769, arXiv:1610.01160
- Gschwend, J., Rossel, A. C., Ogando, R. L. C., et al., 2018, Astronomy and Computing, 25, 58, arXiv:1708.05643
- Guzzo, L., Scoddeggio, M., Garilli, B., et al., 2014, A&A, 566, A108, arXiv:1303.2623
- Guzzo, L., Vipers Team, 2017, The Messenger, 168, 40
- Hartley, W. G., Almaini, O., Mortlock, A., et al., 2013, MNRAS, 431, 4, 3045, arXiv:1303.0816
- Herbel, J., Kacprzak, T., Amara, A., Refregier, A., Bruderer, C., Nicola, A., 2017, JCAP, 2017, 8, 035, arXiv:1705.05386
- Heymans, C., Grocutt, E., Heavens, A., et al., 2013, MNRAS, 432, 2433, arXiv:1303.1808
- Hildebrandt, H., Erben, T., Kuijken, K., et al., 2012, MNRAS, 421, 3, 2355, arXiv:1111.4434
- Hildebrandt, H., Köhlinger, F., van den Busch, J. L., et al., 2018, arXiv e-prints, arXiv:1812.06076, arXiv:1812.06076
- Hinton, S. R., Davis, T. M., Lidman, C., Glazebrook, K., Lewis, G. F., 2016, Astronomy and Computing, 15, 61, arXiv:1603.09438
- Hoyle, B., Gruen, D., Bernstein, G. M., et al., 2018, MNRAS, 478, 1, 592, arXiv:1708.01532
- Joudaki, S., Blake, C., Heymans, C., et al., 2017, MNRAS, 465, 2033, arXiv:1601.05786
- Joudaki, S., Hildebrandt, H., Traykova, D., et al., 2019, arXiv e-prints, arXiv:1906.09262, arXiv:1906.09262
- Kashino, D., Silverman, J. D., Sanders, D., et al., 2017, ApJ, 835, 1, 88, arXiv:1604.06802
- Kohonen, T., 1982, Biological Cybernetics, 43, 1, 59, ISSN 1432-0770
- Le Fèvre, O., Saisse, M., Mancini, D., et al., 2003, Commissioning and performances of the VLT-VIMOS instrument, vol. 4841 of *Society of Photo-Optical Instrumentation Engineers (SPIE) Conference Series*, 1670–1681
- Le Fèvre, O., Tasca, L. A. M., Cassata, P., et al., 2015, A&A,

576, A79, arXiv:1403.3938

Le Fèvre, O., Vettolani, G., Garilli, B., et al., 2005, *A&A*, 439, 3, 845, arXiv:astro-ph/0409133

Leistedt, B., Hogg, D. W., Wechsler, R. H., DeRose, J., 2019, *ApJ*, 881, 1, 80, arXiv:1807.01391

Lilly, S. J., Le Brun, V., Maier, C., et al., 2009, *ApJS*, 184, 2, 218

Lilly, S. J., Le Fèvre, O., Renzini, A., et al., 2007, *ApJS*, 172, 1, 70, arXiv:astro-ph/0612291

Lima, M., Cunha, C. E., Oyaizu, H., Frieman, J., Lin, H., Sheldon, E. S., 2008, *MNRAS*, 390, 1, 118, arXiv:0801.3822

Maltby, D. T., Almaini, O., Wild, V., et al., 2016, *MNRAS*, 459, 1, L114, arXiv:1603.08941

Mandelbaum, R., Seljak, U., Hirata, C. M., et al., 2008, *MNRAS*, 386, 2, 781, arXiv:0709.1692

Masters, D., Capak, P., Stern, D., et al., 2015, *ApJ*, 813, 1, 53, arXiv:1509.03318

Masters, D. C., Stern, D. K., Cohen, J. G., et al., 2017, *ApJ*, 841, 2, 111, arXiv:1704.06665

Masters, D. C., Stern, D. K., Cohen, J. G., et al., 2019, *ApJ*, 877, 2, 81, arXiv:1904.06394

Newman, J. A., 2008, *ApJ*, 684, 1, 88, arXiv:0805.1409

Newman, J. A., Abate, A., Abdalla, F. B., et al., 2015, *Astroparticle Physics*, 63, 81, arXiv:1309.5384

Newman, J. A., Cooper, M. C., Davis, M., et al., 2013, *ApJS*, 208, 1, 5, arXiv:1203.3192

Noll, S., Kausch, W., Barden, M., Jones, A. M., Szyszka, C., Kimeswenger, S., 2013, *The Cerro Paranal Advanced Sky Model*, Tech. rep.

Parkinson, D., Riemer-Sørensen, S., Blake, C., et al., 2012, *Phys.Rev.D*, 86, 10, 103518, arXiv:1210.2130

Rau, M. M., Hoyle, B., Paech, K., Seitz, S., 2017, *MNRAS*, 466, 3, 2927, arXiv:1607.00383

Rau, M. M., Seitz, S., Brimiouille, F., et al., 2015, *MNRAS*, 452, 4, 3710, arXiv:1503.08215

Rau, M. M., Wilson, S., Mandelbaum, R., 2019, *Monthly Notices of the Royal Astronomical Society*, 491, 4, 47684782, ISSN 1365-2966

Sánchez, C., Bernstein, G. M., 2019, *MNRAS*, 483, 2, 2801, arXiv:1807.11873

Sánchez, C., Carrasco Kind, M., Lin, H., et al., 2014, *MNRAS*, 445, 2, 1482, arXiv:1406.4407

Schmidt, S. J., Thorman, P., 2013, *MNRAS*, 431, 3, 2766, arXiv:1211.3245

Scoville, N., Aussel, H., Brusa, M., et al., 2007, *ApJS*, 172, 1, 1, arXiv:astro-ph/0612305

Springel, V., 2005, *MNRAS*, 364, 1105, astro-ph/0505010

Tanaka, M., Coupon, J., Hsieh, B.-C., et al., 2018, *PASJ*, 70, S9, arXiv:1704.05988

Tasca, L. A. M., Le Fèvre, O., Ribeiro, B., et al., 2017, *A&A*, 600, A110, arXiv:1602.01842

Troxel, M. A., MacCrann, N., Zuntz, J., et al., 2018, *Phys.Rev.D*, 98, 4, 043528, arXiv:1708.01538

Wright, A. H., Hildebrandt, H., Kuijken, K., et al., 2018, arXiv e-prints, arXiv:1812.06077, arXiv:1812.06077

Wright, A. H., Hildebrandt, H., van den Busch, J. L., Heymans, C., 2019, arXiv e-prints, arXiv:1909.09632, arXiv:1909.09632

Wuyts, E., Wisnioski, E., Fossati, M., et al., 2016, *ApJ*, 827, 1, 74, arXiv:1603.01139

AFFILIATIONS

- ¹ Department of Physics & Astronomy, University College London, Gower Street, London, WC1E 6BT, UK
- ² Département de Physique Théorique and Center for Astroparticle Physics, Université de Genève, 24 quai Ernest Ansermet, CH-1211 Geneva, Switzerland
- ³ Department of Physics, ETH Zurich, Wolfgang-Pauli-Strasse 16, CH-8093 Zurich, Switzerland
- ⁴ Department of Astronomy and Astrophysics, University of Chicago, Chicago, IL 60637, USA
- ⁵ Kavli Institute for Cosmological Physics, University of Chicago, Chicago, IL 60637, USA
- ⁶ Centro de Investigaciones Energéticas, Medioambientales y Tecnológicas (CIEMAT), Madrid, Spain
- ⁷ School of Mathematics and Physics, University of Queensland, Brisbane, QLD 4072, Australia
- ⁸ Max Planck Institute for Extraterrestrial Physics, Giessenbachstrasse, 85748 Garching, Germany
- ⁹ Universitäts-Sternwarte, Fakultät für Physik, Ludwig-Maximilians Universität München, Scheinerstr. 1, 81679 München, Germany
- ¹⁰ Department of Physics, Stanford University, 382 Via Pueblo Mall, Stanford, CA 94305, USA
- ¹¹ Kavli Institute for Particle Astrophysics & Cosmology, P. O. Box 2450, Stanford University, Stanford, CA 94305, USA
- ¹² SLAC National Accelerator Laboratory, Menlo Park, CA 94025, USA
- ¹³ Laboratório Interinstitucional de e-Astronomia - LIneA, Rua Gal. José Cristino 77, Rio de Janeiro, RJ - 20921-400, Brazil
- ¹⁴ Observatório Nacional, Rua Gal. José Cristino 77, Rio de Janeiro, RJ - 20921-400, Brazil
- ¹⁵ The Research School of Astronomy and Astrophysics, Australian National University, ACT 2601, Australia
- ¹⁶ Australian Astronomical Optics, Macquarie University, North Ryde, NSW 2113, Australia
- ¹⁷ Lowell Observatory, 1400 Mars Hill Rd, Flagstaff, AZ 86001, USA
- ¹⁸ McWilliams Center for Cosmology, Department of Physics, Carnegie Mellon University, Pittsburgh, PA 15213, USA
- ¹⁹ Department of Astronomy, University of California, Berkeley, 501 Campbell Hall, Berkeley, CA 94720, USA
- ²⁰ Santa Cruz Institute for Particle Physics, Santa Cruz, CA 95064, USA
- ²¹ Cerro Tololo Inter-American Observatory, National Optical Astronomy Observatory, Casilla 603, La Serena, Chile
- ²² Departamento de Física Matemática, Instituto de Física, Universidade de São Paulo, CP 66318, São Paulo, SP, 05314-970, Brazil
- ²³ Fermi National Accelerator Laboratory, P. O. Box 500, Batavia, IL 60510, USA
- ²⁴ Instituto de Física Teórica UAM/CSIC, Universidad Autónoma de Madrid, 28049 Madrid, Spain
- ²⁵ Department of Physics and Astronomy, University of Pennsylvania, Philadelphia, PA 19104, USA
- ²⁶ CNRS, UMR 7095, Institut d'Astrophysique de Paris, F-75014, Paris, France
- ²⁷ Sorbonne Universités, UPMC Univ Paris 06, UMR 7095, Institut d'Astrophysique de Paris, F-75014, Paris, France
- ²⁸ Jodrell Bank Center for Astrophysics, School of Physics and Astronomy, University of Manchester, Oxford Road, Manchester, M13 9PL, UK
- ²⁹ Department of Astronomy, University of Illinois at Urbana-Champaign, 1002 W. Green Street, Urbana, IL 61801, USA

³⁰ National Center for Supercomputing Applications, 1205 West Clark St., Urbana, IL 61801, USA

³¹ Institut de Física d'Altes Energies (IFAE), The Barcelona Institute of Science and Technology, Campus UAB, 08193 Bellaterra (Barcelona) Spain

³² Institut d'Estudis Espacials de Catalunya (IEEC), 08034 Barcelona, Spain

³³ Institute of Space Sciences (ICE, CSIC), Campus UAB, Carrer de Can Magrans, s/n, 08193 Barcelona, Spain

³⁴ Physics Department, 2320 Chamberlin Hall, University of Wisconsin-Madison, 1150 University Avenue Madison, WI 53706-1390

³⁵ INAF-Osservatorio Astronomico di Trieste, via G. B. Tiepolo 11, I-34143 Trieste, Italy

³⁶ Institute for Fundamental Physics of the Universe, Via Beirut 2, 34014 Trieste, Italy

³⁷ Department of Physics, IIT Hyderabad, Kandi, Telangana 502285, India

³⁸ Faculty of Physics, Ludwig-Maximilians-Universität, Scheinerstr. 1, 81679 Munich, Germany

³⁹ Department of Astronomy, University of Michigan, Ann Arbor, MI 48109, USA

⁴⁰ Department of Physics, University of Michigan, Ann Arbor, MI 48109, USA

⁴¹ Center for Cosmology and Astro-Particle Physics, The Ohio State University, Columbus, OH 43210, USA

⁴² Department of Physics, The Ohio State University, Columbus, OH 43210, USA

⁴³ Center for Astrophysics | Harvard & Smithsonian, 60 Garden Street, Cambridge, MA 02138, USA

⁴⁴ Department of Astronomy/Steward Observatory, University of Arizona, 933 North Cherry Avenue, Tucson, AZ 85721-0065, USA

⁴⁵ George P. and Cynthia Woods Mitchell Institute for Fundamental Physics and Astronomy, and Department of Physics and Astronomy, Texas A&M University, College Station, TX 77843, USA

⁴⁶ Department of Astrophysical Sciences, Princeton University, Peyton Hall, Princeton, NJ 08544, USA

⁴⁷ Institució Catalana de Recerca i Estudis Avançats, E-08010 Barcelona, Spain

⁴⁸ School of Physics and Astronomy, University of Southampton, Southampton, SO17 1BJ, UK

⁴⁹ Brandeis University, Physics Department, 415 South Street, Waltham MA 02453

⁵⁰ Computer Science and Mathematics Division, Oak Ridge National Laboratory, Oak Ridge, TN 37831

⁵¹ Department of Physics, Duke University Durham, NC 27708, USA

⁵² Department of Physics and Astronomy, Pevensey Building, University of Sussex, Brighton, BN1 9QH, UK

APPENDIX A: FEATURES USED FOR THE RF TRAINING

In Table A1 we list the spectroscopic features used in the RF training described in Sec. 2.4.

APPENDIX B: EFFECT OF FIELD-TO-FIELD VARIANCE: TEST ON VVDS DEEP

In order to remove the impact of field-to-field variance seen in Sec. 3.2 and isolate the bias in the mean redshift purely due to spectroscopic incompleteness, we repeat the analysis using

Table A1. Features used for the RF training.

Wavelength (Å)	Feature
1215.7	Ly α
240.0	NV
1303.0	OI
1334.5	CII
1397.0	SiIV1393+OIV1402
1549.0	CIV1548
1640.0	HeII
1909.0	CIII]
2142.0	NII]
2626.0	FeII
2799.0	MgII
2852.0	MgI
2964.0	FeII
3727.5	[OII]
3933.7	CaK
3968.5	CaH
4101.7	H δ
4304.4	Gband
4340.4	H γ
4861.3	H β
4958.9	[OIIIa]
5006.8	[OIIIb]
5175.0	MgI
5269.0	CaFe
5711.0	MgI
6562.8	H α
6725.0	[SII]6717.0+6731.3

only the main VVDS Deep field (containing 12,932 objects) and a target sample co-located on the sky. The results are shown in Fig. B1, where the lines and symbols have the same meanings as the upper two panels in Fig. 6.

We note that the general shape of the curves in Fig. B1 is qualitatively different from Fig. 6. For the VVDS Deep sample, the bias in mean redshift before re-weighting is much smaller at low flag limits, reflecting the reduced field-to-field variance. The final bias in redshifts after reweighting, however, does not differ significantly from the previous results where the full sample is used. This illustrates that in general, field-to-field variance could largely be corrected for through the re-weighting process (see also H18).

APPENDIX C: COMPARISON WITH GRUEN & BRIMIOULLE (2017)

In order to compare our results on selection bias to real spectroscopic samples, we run an analysis of the type of Gruen & Brimioulle (2017). We use the same catalogues and formalism but with a magnitude cut to match the DES-like sample used in this paper, and with four redshift bins. We do not force the redshift bins to be the same as those in the DES Y1 analysis, instead allowing the bin boundaries in redshift to adapt so that there are equal numbers of spectroscopic objects in each, as was done in Gruen & Brimioulle (2017).

The catalogue used in Gruen & Brimioulle (2017) was constructed from the overlap of the four CFHTLS Deep fields⁹ with near-infrared imaging from the WIRCam Deep Survey (WIRDS, Bielby et al. 2012), which we cut at $i_{\text{CFHT}} < 23.4$. Photometric redshifts are determined by a template fit

⁹ <http://www.cfht.hawaii.edu/Science/CFHLS/cfhtlsdeepwidefields.html>

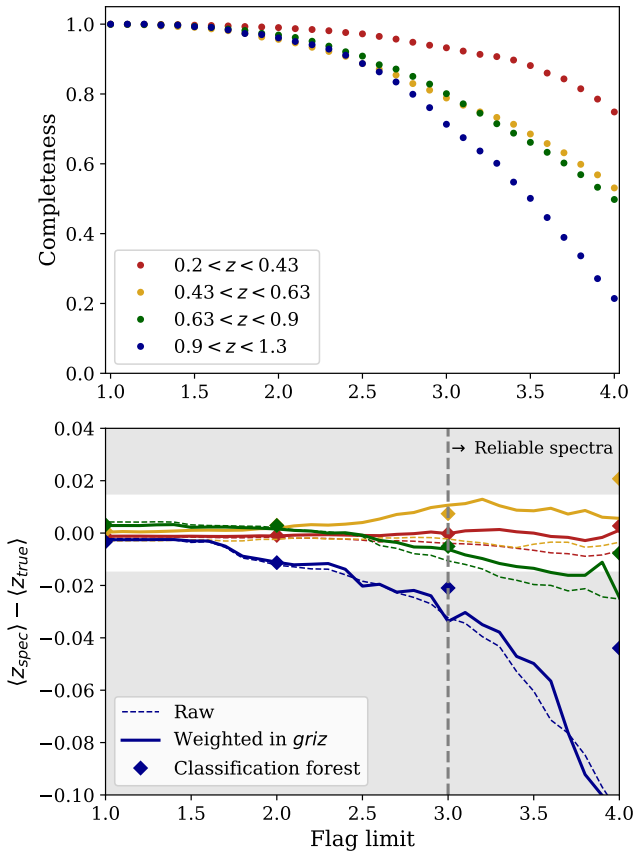


Figure B1. Same as the top two panels of Fig. 6, but for VVDS Deep (field 1) alone.

with Photo- z (Bender et al. 2001) to the *ugriz* CFHT and *JHK_s* WIRDS fluxes. This is the only source of redshift we use in this test, which assumes that the 8-band photometric redshift closely approximates the truth. Typical uncertainties on photo- z from 8-bands covering the u to K -band wavelength range are $\sim 3 - 4\%$ at the depths considered here. See, for instance, Hartley et al. (2013).

Spectroscopic redshift measurements are compiled from the VIMOS VLT Deep Survey (VVDS-Deep, Le Fèvre et al. 2005), the VIMOS Public Extragalactic Survey (VIPERS, Garilli et al. 2014; Guzzo et al. 2014), the VIMOS Ultra Deep Survey (VUDS, Le Fèvre et al. 2015; Tasca et al. 2017), zCOSMOS-bright and zCOSMOS-deep (Lilly et al. 2007), or the Deep Extragalactic Evolutionary Probe-2 (DEEP2) survey (Newman et al. 2013). We mark objects with Flag 3 or 4 as successful spectroscopic redshift determinations and label these as “spectroscopically selected”. Note that VIPERS, zCOSMOS-deep, VVDS and DEEP2 have color-based pre-selection of targets applied (cf. Sec. 3.1) in addition to the purely spectroscopic selection effects primarily studied in this work (Sec. 3.2).

We build a single color-magnitude decision tree by performing splits at the median of whichever of $i, g - i, r - i$ or $i - z$ separates the two subsamples best in redshift. These subsamples, called leaves, are divided further until no additional split significantly separates the subsamples in redshift, or until there are fewer than 10 spectroscopically selected galaxies left in a leaf. These leaves are then ordered by the mean photometric redshift of all galaxies they contain and separated into bins of consecutive leaves such that each contains approximately one quarter of the total number of photometric galaxies. The mean true redshift of each bin is defined

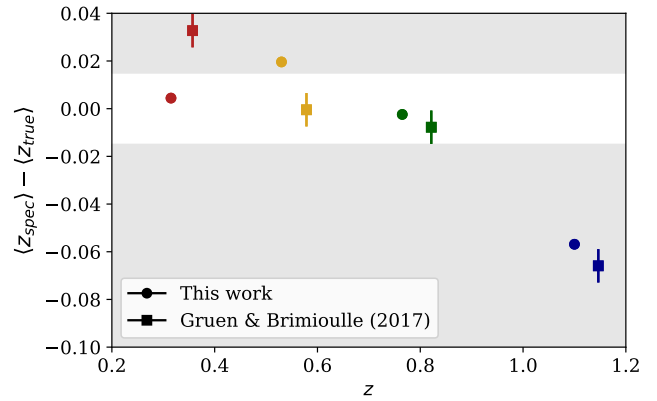


Figure C1. Comparison of the bias in mean redshift found through our simulated data sets in this work and the observed data sets used in Gruen & Brimiouille (2017).

as the mean photometric redshift of all photometric galaxies it contains. We make a second estimate of the mean redshift using the photometric redshifts of the spectroscopically selected objects. When computing this second mean, each spectroscopically-selected galaxy is weighted by the ratio of photometric to spectroscopically-selected galaxies in its leaf. In this way, we emulate reweighting by *griz* color-magnitude to reduce the spectroscopic selection bias.

Fig. C1 shows the difference of these two estimates, i.e. the spectroscopic selection bias, as a function of mean photometric redshift of the bin. Unlike the main result of this paper, this is a mix of the VIMOS-like implicit selection effect of Sec. 3.2 with corresponding effects for DEIMOS/DEEP2 and color pre-selection effects as in Sec. 3.1. Depending on the mix of spectroscopic surveys used, the spectroscopic selection bias found could potentially vary substantially. Despite these differences, the overall amplitude and redshift trend of spectroscopic selection bias is rather similar to the main result of this work.

APPENDIX D: REWEIGHTED COLOUR SPACE

One very basic requirement of the reweighting scheme used in Lima et al. (2008) is that the entire colour-magnitude space of the target data set is sampled by objects with spectroscopic redshifts (albeit poorly in some regions). If it is not, then the photometric distributions cannot be matched, and there would be no reason to believe that the resulting redshift distribution would be representative of the target sample. In Fig. D1 we show the photometric space of the target galaxy sample alongside the weighted and unweighted distributions of objects with successful spectroscopic redshift assignments, for our fiducial case: $\text{Flag} \geq 3$, $i < 23.4$, in the simulations used in Sec. 3. The weights applied to the spectroscopic data do a good job in replicating the photometric space of the target data set. However, as we showed in Sec. 3.2, the redshift distribution is not accurately recovered in all four redshift intervals.

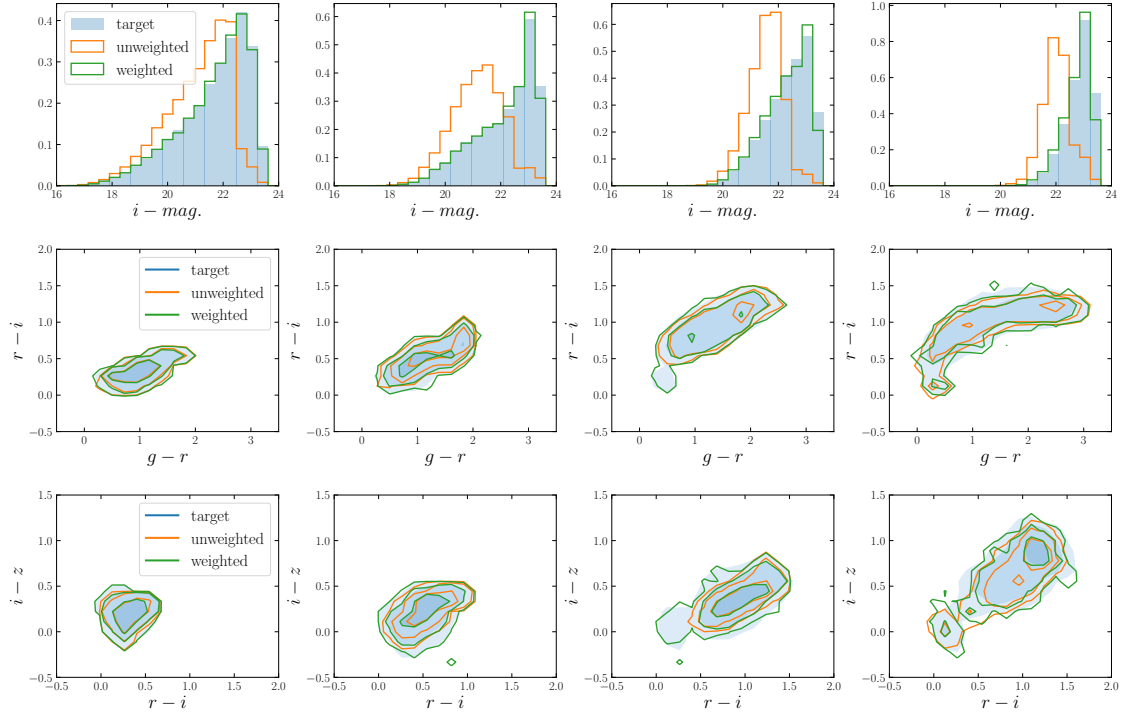


Figure D1. Weighted (green) and unweighted (orange) magnitude and colour-space distributions in our four redshift intervals, compared with the target photometric sample. Distributions are shown for the fiducial case: $i < 23.4$ and spectroscopic Flag ≥ 3 . The weighted spectroscopic sample closely mimics the target photometric sample in terms of their photometric distributions, correcting the mismatch in sampling from the unweighted incomplete spectroscopic sample. Nevertheless, the redshift distribution is not correctly recovered (see Sec. 3.2).